Murine Alveolar Macrophages Rapidly Accumulate Intranasally Administered SARS-CoV-2 Spike Protein leading to Neutrophil Recruitment and Damage

Authors: Chung Park[1], Il-Young Hwang[1], Serena Li-Sue Yan[1], Sinmanus Vimonpatranon [2,3], Danlan Wei[2], Don Van Ryk[2], Alexandre Girard[2], Claudia Cicala[2], James Arthos[2] and John H. Kehrl [1,4]

Affiliations:

[1]B-cell Molecular Immunology Section, Laboratory of Immunoregulation, National Institutes of Allergy and Infectious Diseases, National Institutes of Health, Bethesda, Maryland 20892.

[2]Immunopathogenesis Section, Laboratory of Immunoregulation, National Institute of Allergy and Infectious Diseases, Bethesda, Maryland, United States of America.

[3]Department of Retrovirology, Armed Forces Research Institute of Medical Sciences – United States Component, Bangkok, Thailand [4]Corresponding author.

Running title: Imaging SARS-CoV-2 Spike protein in mice.

To whom correspondence should be addressed: John H. Kehrl, Laboratory of Immunoregulation, National Institute of Allergy and Infectious Diseases, National Institutes of Health, Bldg. 10, Room 6A01, 10 Center Dr. MSC 1876, Bethesda, Maryland 20892, United States of America; Fax: 301-402-0070. Email: jkehrl@niaid.nih.gov

Keywords: alveolar macrophage, SARS-CoV-2, neutrophil, NETosis, Spike protein, Siglec

Abstract: The trimeric SARS-CoV-2 Spike protein mediates viral attachment facilitating cell entry. Most COVID-19 vaccines direct mammalian cells to express the Spike protein or deliver it directly via inoculation to engender a protective immune response. The trafficking and cellular tropism of the Spike protein *in vivo* and its impact on immune cells remains incompletely elucidated. In this study we inoculated mice intranasally, intravenously, and subcutaneously with fluorescently labeled recombinant SARS-CoV-2 Spike protein. Using flow cytometry and imaging techniques we analyzed its localization, immune cell tropism, and acute functional impact. Intranasal administration led to rapid lung alveolar macrophage uptake, pulmonary vascular leakage, and neutrophil recruitment and damage. When injected near the inguinal lymph node medullary, but not subcapsular macrophages, captured the protein, while scrotal injection recruited and fragmented neutrophils. Wide-spread endothelial and liver Kupffer cell uptake followed intravenous administration. Human peripheral blood cells B cells, neutrophils, monocytes, and myeloid dendritic cells all efficiently bound Spike protein. Exposure to the Spike protein enhanced neutrophil NETosis and augmented human macrophage TNF-α and IL-6 production. Human and murine immune cells employed C-type lectin receptors and Siglecs to help capture the Spike protein. This study highlights the potential toxicity of the SARS-CoV-2 Spike protein for mammalian cells and illustrates the central role for alveolar macrophage in pathogenic protein uptake.

Introduction

In 2019 a new coronavirus (SARS-CoV-2) was identified as the cause of an epidemic outbreak of an acute respiratory syndrome in Wuhan, China. SARS-CoV-2 used the same cell entry receptor—angiotensin converting enzyme II (ACE2)—as did SARS-CoV-1 (1). The SARS-CoV-2 Spike protein mediates cell entry and is a single-pass transmembrane proteins that forms homotrimers. It has a large N-terminal ectodomain exposed to the exterior, a transmembrane helix, and a short C-terminal tail located within the virus. Each Spike monomer contains two regions termed S1 and S2. In the assembled trimer the S1 regions contain the receptor binding domain while the S2 regions forms a flexible stalk, which mediates membrane fusion between the viral envelope and the host cell membrane (2-4). The S1 region is divided into a N-terminal domain and C-terminal domain, the latter interacts with the target cell ACE2 (5-11). Like other Coronavirus spike proteins SARS-CoV-2 Spike protein is heavily N-linked glycosylated (12, 13) and blocking N- and O-glycans dramatically reduced viral entry (14). The SARS-CoV-2 Spike proteins is activated by host cell proteases that cleave the protein at the S1-S2 boundary and subsequently at the S2' site (15-17). Because Spike proteins are located on the surface of the virus, they are a major antigen targeted by the host immune system (18).

During natural infection host immune cells encounter Spike proteins via several different avenues. First, by direct contact with Spike protein bearing viral particles released from infected cells. Second, although the SARS-CoV-2 virions assemble in intracellular compartments of infected cells, unincorporated Spike proteins can reach the plasma membrane. Infected cells expressing Spike proteins may bind to cellular receptors present on resident or recruited immune cells. Third, extracellular vesicles (EVs) released by virally infected cells can contain Spike proteins. Mass spectrometry and nanoscale flow cytometry demonstrated SARS-CoV-2 Spike protein incorporation into EVs (19). Fourth, Spike proteins are preprocessed during viral assembly utilizing the furin protease cleavage site between the S1 and S2 subunits (17). When the Spike protein adopts a fusion conformation the ACE2 receptor-binding domain separates from the membrane-bound S2 subunit. Soluble S1 subunits shed from infected cells or from the virions *in vivo* may bind to other cells via ACE2 or other binding partners. Intriguingly 60% of the plasma samples from patients with post-acute sequelae of coronavirus disease 2019 (PASC) had detectable levels of Spike protein using an ultrasensitive antigen capture assay (20). Prolonged exposure to Spike protein has been suggested to be responsible for Long-COVID syndrome (21). Humans also encounter SARS-CoV-2 Spike protein via vaccination (22). Serious adverse events following vaccination are rare but include vaccine-induced immune thrombocytopenia and thrombosis; myocarditis and pericarditis; and a variety of autoimmune illnesses (23). Due to waning effectiveness humans require repeated immunizations to maintain immunity and protection against potentially severe disease raising some concerns about the impact of repeated exposure to the SARS-CoV-2 Spike proteins.

To better understand the localization and trafficking of the SARS-CoV-2 Spike protein following administration and perhaps during natural infection we prepared a recombinant SARS-CoV-2 Spike ectodomain stabilized in a prefusion conformation (24). This variant (S-2P) contained two consecutive proline substitutions in the S2 subunit. This double-proline substitution (SARS-CoV-2 S-2P) has allowed the rapid determination of high-resolution cryo-EM structures. Fluorescently labeled SARS-CoV-2 Spike ectodomain, a D614G variant (25-27), a high mannose (14), and de-glycosylated version were injected into mice to characterize uptake and identify human mononuclear cells that bound these proteins, and to perform functional studies. In some instances, we used viral like particles (VLPs) expressing the full-length Spike protein. Our results identified the *in vivo* cellular tropism of the SARS-CoV-2 Spike proteins, delineated their human mononuclear cell targets, provided insights into their functional effects, thereby, helping afford a basis for understanding their impact on humans.

Results

Preparation of SARS-CoV-2 Spike proteins and VLPs expressing them

We purified a stabilized exodomain of the original SARS-CoV-2 Spike protein (24) using media conditioned by transfected CHO-S or HEK293F cells. Because of higher yields most experiments used CHO-S derived protein. The strategy for producing the recombinant protein is shown (**Figure 1-figure supplement 1**). Based on its mobility on size exclusion chromatography the Spike proteins spontaneously formed trimers. Kifunensine treated cultures were used to generate a high mannose version, and PNGase F treated protein generated an N-glycan deficient version, and they will be referred to as such. The PNGase F treatment resulted in two distinct chromatography peaks that exhibited slightly different mobilities on SDS-PAGE. As discussed below we predominately used the preparation from fractions 9-11. The D614G mutant of the original Wuhan SARS-CoV-2 Spike protein was also purified. Each of the recombinant proteins was subjected to two rounds of Triton X-114 extraction to remove any residual lipopolysaccharide (28). The N-termini of the recombinant proteins were labeled with Alexa Fluor 488. In some experiments we used viral like particles (VLPs) that expressed the original Wuhan Spike protein. We produced the VLPs using HEK293T cells along with a plasmid encoding the human immunodeficiency GAG protein fused to green fluorescent protein (GFP) and a full-length SARS-CoV-2 Spike protein expression vector. Mice received the Spike protein preparations or the SARS-CoV-2 VLPs by intranasal instillation, while only the Spike proteins were injected intravenously or subcutaneously.

Instillation of SARS-CoV-2 Spike proteins and Spike protein expressing VLPs affects the lung cellular composition and architecture

106 At various time points after Spike protein or VLP nasal instillation lungs from mice were processed for
107 confocal microscopy. A Siglec-F antibody identified alveolar macrophages (AMs) while CD169 (Siglec-1)
108 immunostaining delineated a subset of large airway associated macrophages (29). Interstitial and
109 inflammatory macrophages do not express Siglec-F. At 3 hours post instillation low magnification images
110 of mouse lung sections revealed Spike protein (Trimer) uptake by Siglec-F positive cells. Due to the uneven
111 distribution of the instilled Spike protein the Siglec-F positive cells in the lower portion of the image lack
112 signal (**Figure 1A, Figure 1-figure supplement 2A**). The Siglec-F positive macrophages located near the
113 bronchial epithelium and in the nearby alveoli initially accumulated the labeled protein **(Figure 1B)**. Even
114 at the 30-minute time point AMs had already accumulated it **(Figure 1C)**. Most of the macrophages that
115 acquired the Spike proteins were Siglec-F positive, lacked CD169 **(Figure 1D)**, but were wheat germ
116 agglutinin positive, a mucin marker **(Figure 1E)**. Repeating the experiment but substituting the Spike
117 protein with VLPs expressing the SARS-CoV-2 Spike protein revealed a similar pattern of uptake by AMs,
118 but with greater neutrophil recruitment and granulation compared to delta Env VLPs. **(Figure 1F, Figure**
119 **1-figure supplement 2B, C)**. Immunostaining with LYVE-1 and CD31 to identify the lymphatic and blood
120 vessel endothelium, respectively, **(Figure 1G)** or with Podoplanin another lymphatic endothelial cell
121 marker **(Figure 1H, Figure 1-figure supplement 2D)** showed the rapid accumulation of the Spike protein
122 bearing VLPs in small and large lymphatic vessels. Within 3 hours of administration of either the VLPs
123 **(Figure 1I)** or the Spike protein (data not shown) areas of alveolar collapse and lung damage were evident.
124 To assess the cellular response to Spike protein instillation and to delineate the cells that had
125 acquired Spike protein *in vivo* we collected mouse lungs 18 hours post exposure to different SARS-CoV-2
126 Spike protein preparations. Saline instillation served as a control. Lung fragments were digested, and then
127 pushed through a 40-micron cell strainer. Analysis of the collected cells by flow cytometry revealed that
128 the SARS-CoV-2 Spike protein increased the number of neutrophils, monocytes, and dendritic cells in the
129 lung, but did not affect lymphocyte or eosinophil numbers **(Figure 2A)**. Due to the uneven distribution of
130 the instilled protein and because of their rapid turnover the neutrophil numbers likely underestimate the
131 local neutrophil recruitment. As the imaging experiments indicated AMs most avidly acquired the Spike
132 protein, some interstitial macrophages also retained it, while only a low percentage of the lung neutrophils
133 and dendritic cells were positive following isolation **(Figure 2B)**. Instillation of the glycan deficient Spike
134 protein reduced the monocyte cellular infiltrate and decreased the % of alveolar macrophages that retained
135 the protein. The high mannose Spike protein slightly increased the numbers of neutrophil and macrophages
136 in the lung despite a lower uptake by alveolar and interstitial macrophages. Finally, the D614G mutation
137 reduced the cellular infiltrate compared to the unmutated protein and had a slightly different cell binding
138 profile as a greater percentage of monocytes, eosinophils, and dendritic cells retained it **(Figure 2A, B)**. We
139 also tested whether the addition of human ACE2 affected the cellular uptake of the Spike protein following

140 intranasal administration by comparing wild type and the human ACE2 transgenic mice. While we saw
141 little difference by imaging, we did note some minor changes in the cellular uptake pattern, most notably
142 an increase uptake by AM and decrease by interstitial macrophages **(Figure 2-figure supplement 1)**
143

144 **Altered lung vascular permeability, neutrophil recruitment, and lung damage 3 hours post**
145 **instillation of the Spike protein**

146 The increase lung leukocytes following the Spike protein nasal instillation suggested that it may have
147 altered the vascular permeability of the lung. To assess whether vasculature permeability changes had
148 occurred, we intravenously injected Evans blue dye, which in the absence of a permeability defect remains
149 confined to the vasculature (30). Prior to injecting the Evans blue, we instilled in the nasal cavity the SARS-
150 CoV-2 Spike protein, the S1 subunit of the HCoV-HKU1 Spike protein, or a saline control. Inspection of
151 the lungs from the SARS-CoV-2 spike protein treated mice revealed a strong increase in Evan blue staining
152 while the lungs from the S1 subunit HCoV-HKU1 treated mice had a minimal increase. Quantifying the
153 Evans blue dye in collected lungs and liver confirmed the increase in vasculature permeability in the lungs
154 of the SARS-CoV-2 Spike protein treated mice **(Figure 3A).** Next, we compared the S1 subunit of SARS-
155 CoV-2 Spike protein to the HCoV-HKU1 S1 subunit. The S1 subunit preparations were purified from
156 transfected HEK 293 cells. The results of administrating the S1 subunit of HCoV-HKU1 Spike protein did
157 not differ from the saline control while the S1 subunit from SARS-CoV-2 like the SARS-CoV-2 trimer
158 increased the lung vascular permeability to Evans blue (**Figure 3-figure supplement 1A)**. We also tested
159 whether the presence of hACE2 affected the response by using K18-hACE2 transgenic mice as the
160 recipients. The presence of the K18-hACE2 transgene slightly increased the lung vasculature permeability
161 upon SARS-CoV-2 trimer instillation **(Figure 3- figure supplement 1B).** Consistent with the increase in
162 lung vascular permeability 3 hours post SARS-CoV-2 Spike protein instillation, Siglec-F positive lung
163 macrophages bearing the Spike protein were surrounded by neutrophils and neutrophil fragments **(Figure**
164 **3B, C**).

165 Next, we investigated the potential impact of modifying the glycans displayed by the spike proteins
166 on lung vasculature homeostasis and neutrophil recruitment. Imaging fixed lung tissue from mice instilled
167 with saline, SARS-CoV-2 Spike protein, glycan-deficient protein, high mannose protein, and the HCoV-
168 HKU1 S1 subunit recombinant protein revealed enhanced neutrophil recruitment with each SARS-CoV-2
169 Spike protein preparation. We analyzed the neutrophil count in a 200 × 200 μm² area at six different
170 locations. The surveyed areas of the SARS-CoV-2 Spike protein instilled mice had approximately a 6.5-
171 fold higher neutrophil density compared to the saline-treated control mice. The high mannose version of
172 the Spike protein recruited fewer neutrophils at the three-hour time point while the PNGase F treated version
173 did not differ from the untreated trimer **(Figure 3D, Figure 3- figure supplement 1C)**.

174 **Neutrophil recruitment and damage in the cremaster muscle following local protein injection, and**
175 **in the liver following intravenous injection**

176 An exteriorized cremaster muscle is commonly used to intravitally image mouse neutrophil transmigration
177 and interstitial motility (31). Although this model lacks Siglec F-positive macrophages, it is worth
178 monitoring the effect of the SARS-CoV-2 Spike protein on neutrophils recruited into an inflammatory site.
179 Within 3 hours local IL-1β injection recruits bone marrow neutrophils and leads to their transmigration into
180 the nearby tissue. Co-injecting fluorescently labeled Ly6G and Gp1bβ antibodies identified neutrophils and
181 platelets, respectively. Local PBS injection and intermittent imaging over a 6-hour time frame revealed
182 occasional blood neutrophil and numerous flowing platelets **(Figure 4A, Video 1)**. Local intrascrotal
183 injection of unlabeled SARS-CoV-2 Spike protein caused a modest recruitment of neutrophils at 4-6 hours
184 post injection **(Figure 4A, Figure 4-figure supplement 1, Video 1)**. To better assess the long-term effect
185 of the SARS-CoV-2 Spike protein, we co-injected Il-1β and waited until the following day to image.
186 Typically, at 24 hours post Il-1β the inflammatory response is resolving, and the interstitial neutrophil
187 numbers are declining from their peak **(Video 2)**. In contrast, each of the Spike protein preparations
188 adversely affected neutrophil motility and morphology. Numerous neutrophils and neutrophil fragments
189 localized along the blood vessel walls and were scattered within the interstitium **(Figure 4B, Video 2)**. We
190 did not note any significant difference between the different SARS-CoV-2 Spike protein preparations as
191 each caused neutrophil fragmentation and a decline in mobile neutrophils **(Figure 4C)**.

192 We also assessed the impact of injecting the labeled SARS-CoV-2 protein into the blood on the
193 liver sinusoids using intravital microscopy. Snapshots at three hours post infusion revealed Spike protein
194 outlined liver sinusoid endothelial cells co-localized with the CD31 delineated sinusoid endothelial
195 membranes. Kupffer cells identified by F4-80 immunostaining rapidly acquired large amounts of the
196 infused Spike protein **(Figure 4-figure supplement 2A, Video 3)**. The sinusoids, normally devoid of
197 neutrophils, contained many $Ly6G^{+}$ neutrophils. However, by 18 hours post infusion the amount of Spike
198 protein outlining the sinusoids had declined as had the Kupffer cell associated material **(Figure 4-figure**
199 **supplement 2B)**. The neutrophil infiltration had largely resolved suggesting that the inflammatory signals
200 had declined. The origin of the white dots interspersed between the sinusoids is unknown, but they were
201 not present at 3 hours post infusion despite identical imaging conditions. One possibility is that altered
202 vascular permeability had allowed some labeled antibodies to leak into the liver parenchyma. To determine
203 whether other endothelial beds also acquired intravenous administered Spike protein we examined the
204 spleen, heart ventricle, and Peyer's patches. At 3 hours post infusion endothelial cells at these three sites
205 had acquired the labelled Spike proteins, most prominently in Peyer's patches **(Figure 4-figure supplement**
206 **3A, B, C)**. Finally, we intravitally imaged the inguinal lymph node at 3 and 18-hour after local injection.

207 Typically, locally injected material rapidly enters nearby afferent lymphatics for delivery to the lymph node
208 where subcapsular sinus macrophages first encounter it (32). If it bypasses these macrophages lymph borne
209 material flows into the lymph node medullary region, where medullary macrophages reside **(Figure 4-**
210 **figure supplement 3D)**. At both the 3-hour time point (data not shown) and at 18 hours subcapsular
211 macrophages showed little interest in the Spike protein, but medullary macrophages avidly acquired it. In
212 contrast to the liver, we did not detect neutrophil recruitment into the lymph node at either time point after
213 tail-base injection.
214

215 **Murine and human neutrophils NETosis following exposure to the SARS-CoV-2 Spike protein**

216 Live cell imaging of lung sections following intranasal instillation of the Spike protein revealed ongoing
217 neutrophil damage and likely NETosis (**Figure 5A**). Time-lapse images show several disrupted neutrophils
218 near a Siglec-F positive AM along with Spike protein bound to a dying neutrophil. This observation along
219 with the cremaster muscle imaging suggested direct neutrophil toxicity. Furthermore, a previous study had
220 shown Spike protein induced neutrophil NETosis (33). To confirm that the Spike protein can trigger
221 neutrophil NETosis and to compare different Spike protein preparations, we briefly exposed murine bone
222 marrow neutrophils and assessed the % of cells undergoing cell death using a flow-based assay. Exposure
223 to fMLP served as a positive control. The lowest concentration of Spike protein (0.1 μg) tested increased
224 the number of dying neutrophils **(Figure 5B)**. Switching to human neutrophils purified from human
225 peripheral blood, exposure to TNFα, LPS or PMA for 4 hours or overnight reduced their viability as
226 expected. Addition of SARS-CoV-2 or the D614G mutant protein (1 μg/ml) decreased their viability at 4
227 hours and more dramatically upon overnight exposure. The high mannose versions of the Spike protein and
228 D614G Spike had a slightly greater toxicity at 4 hours but had a similar impact in the overnight assay
229 **(Figure 5C)**. Finally, we imaged human neutrophils overlaid on SARS-CoV-2 Spike protein treated A549
230 cells, a human lung epithelial cell line. Numerous dying neutrophils could be observed likely undergoing
231 NETosis **(Figure 5D, Video 4)**. These results confirm that the SARS-CoV-2 Spike protein can cause
232 neutrophil damage potentially exacerbating the inflammatory response.
233

234 **Human peripheral blood monocytes, B cells, neutrophils, and dendritic cells bind the SARS-CoV-2**
235 **Spike protein**

236 Next, we assessed human peripheral blood leukocyte binding using the fluorescently labeled Spike protein.
237 Binding assays were performed on ice to avoid endocytosis using Hanks balanced salt solution with added
238 Ca^{2+} and Mn^{2+}, or with EDTA to assess cation dependence. Representative CD4 T cell, B cell, Monocyte,
239 or neutrophil flow patterns using either the Spike protein or the high mannose version are shown **(Figure**

240 **6A)**. The flow cytometry results demonstrated that cations enhanced leukocyte binding particularly so with
241 the high mannose protein. The SARS-CoV-2 S1 protein bound better than did the HKU1 S1 protein, most
242 evident with NK cells, neutrophils, monocytes, and dendritic cells **(Figure 6B)**. The SARS-CoV-2 Spike
243 protein bound better than did the S1 protein with B cells, neutrophils, and monocytes exhibiting the best
244 binding. The high mannose protein bound less well to the different leukocyte subsets. Surprisingly CD4 T
245 cells poorly bound each of the proteins, irrespective of the presence or absence of cations. The D614G
246 Spike protein bound better to neutrophils and monocytes than did the wild-type Spike protein (**Figure 6B**).
247

248 **Murine and human cells use Siglecs to help capture the SARS-CoV-2 Spike Protein**

249 Since murine and human leukocytes lack significant ACE2 levels, the major entry receptor for SARS-CoV-
250 1 and -2, they likely use other receptors to capture the Spike proteins. The strong co-localization with
251 Siglec-F expressing murine AMs prompted an examination of the role of Siglec-F and other Siglecs in
252 capturing the Spike proteins. Siglecs are transmembrane proteins that exhibit specificity for sialic acids
253 attached to the terminal portions of cell-surface glycoproteins. Several viruses take advantage of sialic acid-
254 Siglec interactions for cell targeting, spreading, and trans-infection (34-36). Initially, we established a bead
255 assay to assess the binding to SARS-CoV-2 Spike proteins. We coupled the S1 domain protein, the SARS-
256 CoV-2 stabilized Spike protein, or the PNGase F treated Spike protein and reacted the beads with
257 fluorescently labeled antibody or different recombinant proteins. Flow cytometry analysis revealed strong
258 binding of the Spike protein antibody, human ACE2, but not murine ACE2 as expected **(Figure 7A)**. Siglec-
259 F also bound well, while the human Siglec-5 and Siglec-8 bound poorly despite being the structural and
260 functional equivalents of Siglec-F, respectively (37). Of note the PNGase F treated fraction we used likely
261 retained some N-linked glycans as it remained able to bind ACE2 although it lost Siglec-F binding (Figure
262 7A).

263 Despite the poor binding to the recombinant human Siglecs in the bead assay, we elected to test
264 them in context of a human cell by expressing them in HEK293 cells. We chose HEK293 cells as they
265 exhibited little Spike protein binding. We established ACE2, Siglec5, Siglec-8, Siglec-5/8, ACE2/Siglec-5,
266 and ACE2/Siglec-8 expressing cell lines **(Figure 7B)**. The ACE2 transfected cells behaved as anticipated
267 binding the original Spike protein and even better the D614G version; and binding the S1 protein. The high
268 mannose and glycan deficient Spike proteins bound poorly. In contrast to the bead assay both the Siglec-5
269 and the Siglec-8 expressing HEK293 cells bound the Spike protein, although less efficiently than did the
270 ACE2 expressing cells. They bound the D614G version less well, and very weakly bound the S1 domain
271 protein. The high mannose and glycan deficient Spike proteins exhibited little binding to the Siglec
272 expressing cells. Co-expression of Siglec-5 and -8 did not improve binding, although the ACE2/Siglec co-
273 expressing cells bound the SARS-CoV-2 Spike protein slightly better than did ACE2 only cells. We also

imaged the Siglec-5 expressing HEK293 with labeled protein **(Figure 7C)**. The imaging revealed efficient uptake and Spike protein endocytosis. Co-cultured ACE2 and Siglec-5 expressing cells both captured the Spike protein while HEK293 cells not expressing either protein failed to bind or uptake it **(Figure 7D, Video 5)**. To determine whether Siglec-5 or Siglec-8 could contribute to viral transduction, we produced lentiviral particles expressing the Spike protein from SARS-CoV-2, HKU1, or 229E and attempted to transduce the HEK293 ACE2 expressing cells. Successful transduction resulted in GFP expression, which we quantitated by flow cytometry and only occurred with the lentiviral particles with SARS-CoV-2 Spike protein incorporation **(Figure 7E)**. Both a receptor binding domain antibody and recombinant ACE2 blocked transduction. Recombinant human Siglec-5 partially inhibited although it required relatively high concentrations, while human Siglec-1, human Siglec-2, and murine Siglec-F had no impact on the transduction frequency.

Increased TNF-α and IL-6 production by human macrophages exposed to the SARS-CoV-2 Spike proteins.

Dysregulated cytokine production contributes to the pathogenesis of severe COVID-19 infections (38, 39). To assess whether the Spike proteins can affect macrophage cytokine profiles we cultured human monocytes using conditions that generate M0, M1, or M2 macrophages and treated them with different Spike protein preparations. We collected cell supernatants two days later and measured a panel of known macrophage derived cytokines by ELISA **(Figure 8)**. We found little induction of IL-1β in the cell supernatant indicating that the Spike proteins alone did not trigger the inflammasome activation in these macrophages. In contrast, we did observe significant increases in TNF-α and IL-6 secretion by the original SARS-CoV-2 Spike protein treated macrophages irrespective of whether it was produced in CHO or HEK293F cells. The spike protein produced in HEK293F is predicted to contain more complex carbohydrates than that expressed in CHO cells. While both preparations increased IL-6 and TNF-α production, the spike protein produced by HEK293F cell elicited more TNF-α and less IL-6 compared with the CHO produced spike protein. The spike protein produced in CHO cells treated with Kifunesine elicited a similar cytokine profile as did the spike protein produced in CHO cells in the absence of Kifunesine. The addition of the HKU1 S1 protein did not modify cytokine production by any of the macrophage subsets.

Discussion

This study analyzed the cell tropism of the SARS-CoV-2 Spike protein and some of its variants using fluorescently labeled proteins, flow cytometry, and mice to assess *in vivo* binding. The intranasal

306 administration of SARS-CoV-2 Spike protein to mice led to its rapid uptake by Siglec-F positive AMs and
307 an increased the number of neutrophils, monocytes, and dendritic cells in the lung 18 hours after instillation.
308 Modifying the carbohydrate content of the Spike protein or using a Spike protein with a D614G mutation
309 slightly altered the cell recruitment pattern. The high mannose Spike protein purified from the Kifunensine
310 treated CHO cells increased the number of lung macrophages at 18 hours despite a lower % of macrophages
311 having retained it. As alveolar macrophages express the mannose receptor (MR, CD206), a member of the
312 C-type lectin (CLEC) family, perhaps the high mannose Spike protein is more rapidly endocytosed and
313 degraded accounting for a lower percentage of cells retaining it. This receptor binds high-mannose
314 structures present on the surface of pathogens helping to neutralize them by phagocytic engulfment. Other
315 cell types including immature dendritic cells (DCs), and endothelial cells in hepatic, splenic, lymphatic,
316 and dermal microvasculature express the mannose receptor and would be expected to be targeted by the
317 high mannose Spike protein. We confirmed Siglec-F as a capturing receptor, as it efficiently bound to the
318 S1 domain, and the SARS-CoV-2 Spike protein. Yet alveolar macrophages employ additional receptors to
319 capture the Spike protein as they still accumulated the PNGase F treated Spike protein, which had lost
320 binding to Siglec-F.

321 Arguing against a role for mSiglec-1, $CD169^+$ lung macrophages and $CD169^+$ subcapsular sinus
322 macrophages failed to accumulate the Spike protein *in vivo*. The closest human paralog of mouse Siglec-F
323 is hSiglec-8 (40). While expressed on human eosinophils and mast cells, human AMs apparently lack it. In
324 contrast, human AMs do express Siglec-5 (37). Along with its paired receptor, hSiglec-14, Siglec-5 can
325 modulate innate immune responses (41). When tested in a bead binding assay, in contrast to Siglec-F, neither
326 hSiglec-5 or -8 bound the recombinant Spike protein, yet their expression in a cellular context allowed
327 binding. Additionally, recombinant hSiglec-5 partially inhibited the transduction of Spike protein bearing
328 viral like particles into ACE2 expressing HEK293 cells. Evidently the recombinant protein binding assay
329 we employed did not fully capture the properties of hSiglec-5 or hSiglec-8 in a cellular context. A recent
330 study of human lungs revealed scant alveolar ACE2 expression, highlighting the importance of alternative
331 Spike protein receptors (42). *Ex vivo* infected human lungs and COVID-19 autopsy samples showed AMs
332 positive for SARS-CoV-2 and single-cell transcriptomics revealed nonproductive virus uptake, and
333 activation of inflammatory and anti-viral pathways. Another study which analyzed pulmonary cells from
334 COVID-19 patients found that myeloid cell C-type lectin engagement induced a robust proinflammatory
335 responses that correlated with COVID-19 severity (43). The robust Spike binding to AMs and their potential
336 roles in COVID-19 lung infection warrants a further exploration of their Spike protein binding partners.

337 The intranasal administration of the Spike protein resulted in an increase in lung vascular
338 permeability and local tissue damage. While the mechanisms are unknown, infectious agents that target
339 AMs can trigger the secretion of factors that disrupt the integrity of the pulmonary microvascular cell

340 barrier. For example, Porcine reproductive and respiratory syndrome virus infected AMs trigger
341 transcriptional changes in genes in co-cultured microvascular endothelial cells that reduce vascular integrity
342 (44). Lung endothelial cells may also be directly targeted (45). Spike protein/ACE2 interactions reduce
343 endothelial cell ACE2 expression, which can alter vascular permeability. Yet, the low affinity of mouse
344 ACE2 for the SARS-CoV-2 Spike protein presumably precludes this mechanism in this study. Also arguing
345 against a role for ACE2 in our model, the responses to intranasal Spike protein in human ACE2 transgenic
346 mice resembled those of wild type mice. The Spike protein RGD (Arginine-Glycine-Aspartic Acid) motif
347 can also bind $\alpha_V\beta_3$ integrins present on endothelial cells (46). This affects VE-cadherin function and
348 vascular integrity. However, we did not detect any Spike protein on the pulmonary blood vessels following
349 intranasal administration although a low level of binding may have escaped visualization. In sum, the rapid
350 and intense uptake of Spike protein by AMs supports a role for these cells in the localized neutrophil
351 recruitment, nearby tissue damage, and increased vascular permeability that follows its intranasal
352 administration.

353 The intravenous administration of the Spike protein, led to its accumulation by Kupffer cells in the
354 mouse liver. This uptake was accompanied by a transitory increase in liver sinusoid neutrophils. Human
355 Kupffer cells express LSECtin (liver Siglec and lymph node sinusoidal endothelial cell C-type lectin,
356 CLEC4G) a C-type lectin receptor encoded within the L-SIGN/DC-SIGN/CD23 gene cluster. LSECtin acts
357 as a pathogen attachment factor for Ebola virus and the SARS coronaviruses suggesting that it contributed
358 to the Kupffer cell uptake we noted (47). The liver sinusoid endothelial cells also avidly accumulated the
359 Spike protein. These cells express another C-type lectin receptor L-SIGN (CD209L/CLEC4M), which has
360 been shown to interact in a Ca^{2+}-dependent manner with high-mannose–type N-glycans on the SARS-CoV-
361 2 Spike protein (48). Based on our mouse studies, blood borne SARS-CoV-2 Spike proteins, viral particles,
362 or exosomes bearing the Spike protein are likely to accumulate in the liver during severe or prolonged
363 COVID-19 infection.

364 Local injection of the Spike protein in the region of the cremaster muscle recruited low numbers of
365 neutrophils, but co-administration with IL-1β caused severe neutrophil damage. The Spike protein also
366 proved toxic to purified mouse and human neutrophils cultured *ex vivo* in its presence. Most human
367 neutrophils bound the recombinant Spike protein. The presence of cations in the binding buffer substantially
368 enhanced the binding suggesting that a cation dependent receptor accounted for a significant portion of the
369 binding. While the high mannose version bound neutrophils less well, in the NETosis assay it produced a
370 similar level of neutrophil cell death. Neutrophils likely employ several different receptors to capture the
371 Spike protein. Human neutrophils express several C-type lectin receptors including CLEC5A, which has
372 been implicated in SARS-CoV-2 triggered neutrophil NETosis (49). They also express Siglec-5 (37), which
373 bound the Spike protein when expressed in HEK293 cells.

374 We also assessed the binding of various Spike protein preparations to human peripheral blood
375 mononuclear cells and their impact on cytokine production by M0, M1, and M2 human monocyte derived
376 macrophages. Monocytes, neutrophils, and B cells bound the full-length trimer best, while T and NK cells
377 exhibited little binding. All the cellar subsets bound more of the SARS-CoV-2 Spike protein in the presence
378 of cations arguing for a major role for cation dependent receptors. The high mannose Spike protein bound
379 less well to all tested cell types and its binding exhibited the highest cation dependence. Among the eight
380 cytokines measured in the supernatants conditioned by human monocyte derived macrophages treated with
381 Spike proteins only TNF-α and IL-6 were elevated compared to untreated or HKU1 S1 treated cells. We
382 found little or no change in IL-1β levels suggesting that the tested Spike protein preparations did not activate
383 inflammasomes. Nor did we find any material difference between recombinant Spike protein prepared from
384 HEK293F and CHO cells. Further studies are needed to identify the monocyte, neutrophil, and B cell
385 receptors that account for the Spike protein binding and additional functional studies to assess the
386 consequences of that binding.

387 Several conclusions can be drawn from this study. First, instilled SARS-CoV-2 Spike protein and
388 VLPs bearing the Spike protein rapidly accumulated on mouse AMs suggesting a similar uptake by human
389 alveolar macrophages during an active SARS-CoV-2 infection. In mice, the nasal instillation of the Spike
390 protein is accompanied by lung leukocyte infiltration. Second, murine alveolar macrophages likely use
391 Siglec-F as a capturing receptor although other receptors contribute. Third, following nasal instillation of
392 the Spike protein, the integrity of the pulmonary vasculature weakens. Fourth, resident and recruited
393 neutrophils suffer, either directly targeted by the Spike protein, or secondarily due to the inflammatory
394 response. A similar scenario would be expected during SARS-CoV-2 infection, following direct instillation
395 of the Spike protein in the upper airway of humans, or following an intranasal vaccine that directs the
396 synthesis of the SARS-CoV-2 Spike protein or fragments. Fifth, blood monocytes, B cells, neutrophils, and
397 dendritic cells efficiently bind the Spike protein, while only a low percentage of CD8 T cells and even fewer
398 CD4 T cells do. Spike protein binding to human monocyte derived macrophages increases the TNF-α and
399 IL-6 secretion. Sixth, altering the glycan composition of the Spike and the D614G mutation had surprisingly
400 little impact on the initial inflammatory response. Seventh, viral particles and soluble Spike protein that
401 spills into the blood during SARS-CoV-2 infection or following immunization will likely be cleared by
402 liver Kupffer cells but will also target blood vessel endothelial cells in multiple organs. Finally, injection of
403 the Spike protein as occurs following vaccination rapidly delivers it to the draining lymph node via afferent
404 lymphatics. Surprisingly, lymph node medullary macrophages, which largely serve a degradative function,
405 preferentially uptake the Spike protein. Designing a less toxic Spike protein immunogen that targets
406 subcapsular sinus macrophages might better deliver the immunogen to B cells, thereby eliciting a more
407 efficacious antibody response.

408

409 **Material and Methods**

410 **Mice**

411 C57BL/6 and K18-ACE2 transgenic mice were obtained from Jackson Laboratory. All mice were used in
412 this study were 8-12 weeks of age. Mice were housed under specific-pathogen-free conditions. All the
413 animal experiments and protocols used in the study were approved by the NIAID Animal Care and Use
414 Committee (ACUC) at the National Institutes of Health.

415

416 **Cells**

417 To isolate mouse lung cells, lungs were carefully collected and gently teased apart using forceps into RPMI
418 1640 media containing 2 mM L-glutamine, antibiotics (100 IU/ml penicillin, 100 μg/ml streptomycin), 1
419 mM sodium pyruvate, and 50 μM 2-mercaptoethanol, pH 7.2. The tissue was then digested with Liberase
420 Blendzyme 2 (0.2 mg/ml, Roche Applied Science) and DNase I (20 μg/ml) for 1hr at 37°C. The proteases
421 were inactivated by adding 10% fetal bovine serum and 2 mM EDTA and the cell disaggregated by passing
422 them through a 40 μm nylon sieve (BD Bioscience). Single cells were then washed with 1% Bovine serum
423 albumin (BSA) in PBS and blocked with anti-Fcγ receptor (BD Biosciences). Human peripheral blood
424 mononuclear cells (PBMC) were purified from whole blood by density gradient centrifugation
425 (FicollPaque™, Miltenyi Biotec). Whole blood was collected from healthy donors through an NIH
426 Department of Transfusion Medicine (DTM)-approved protocol (Institutional Review Board of the
427 National Institute of Allergy and Infectious Diseases [NIAID]). Neutrophil and monocyte cell population
428 were each obtained by negative selection (>97% purity, Stem Cell Technologies). To generate human
429 monocyte-derived macrophages, purified monocytes were treated for 7 days with 50 ng/ml human
430 recombinant M-CSF (PeproTech) in RPMI medium supplemented with 10% heat inactivated fetal bovine
431 serum, and 1mM Sodium Pyruvate, 100U Penicillin-Streptomycin (Gibco, ThermoFisher Scientific) in
432 ultra-low attachment culture 100mm dishes. On day 7 the mature macrophages were collected and verified
433 to be more than 90% $CD68^+$ by flow cytometry.

434

435 **Reagents**

436 See reagent table**.**

437

438 **Flow Cytometry**

439 Single cells were re-suspended in 0.1% fatty acid free BSA-Hanks' Balanced Salt Solution (HBSS) with
440 100 μM CaCl2 and 1 mM MnCl2 unless otherwise specified. Buffer without divalent cations included 10
441 mM EDTA. The cells were stained with fluorochrome-conjugated antibodies against various cell surface
442 markers or with different fluorochrome-conjugated proteins, which are listed in the resource and reagent
443 tables in the supplement. LIVE/DEAD™ Fixable Aqua Dead Cell Stain Kit, LIVE/DEAD™ Fixable
444 NearIR Dead Cell Stain Kit or LIVE/DEAD™ Fixable Yellow Dead Cell Stain Kit (Thermo Fisher) were
445 used in all experiments to exclude dead cells. Compensation was performed using AbC™ Total Antibody
446 Compensation Bead Kit (Thermo Fisher) and ArCTM Amine Reactive Compensation Bead (Thermo
447 Fisher) individually stained with each fluorochrome. Compensation matrices were calculated with
448 FACSdiva software. Data acquisition included cell number count was done on a FACSCelesta SORP (BD)
449 flow cytometer and analyzed with FlowJo 10.8.x software (Treestar).
450

451 **Human macrophage polarization and cytokine profiling**

452 To polarize human macrophages, monocyte derived macrophages were plated in 48 well plates at 5×10^4
453 cells per well in 500μl RPMI medium and allowed to rest 2hours at 37°C before treat of cytokines or LPS.
454 The human M0 macrophages were either left untreated or treated for 48h to induce macrophage
455 polarization: (i) for M1 polarization with 10 ng/mL LPS (E055:B55; Sigma-Aldrich) and 20 ng/mL IFNγ
456 (PeproTech), (ii) for M2 polarization with 50 ng/ml human recombinant M-CSF, 20 ng/ml human
457 recombinant IL-4, and 20 ng/ml human recombinant IL-13 (PeproTech). Human macrophages were then
458 cultured alone or with 0.1ug, or 1ug SARS-CoV-2 Spike proteins for 48 hr. The cultured supernatants were
459 collected, and cytokine levels determined using the bead-based immunoassays LEGENDplex™ Human
460 Macrophage/ Microglia Panel (Biolegend). The assays were performed in 96-well plates following the
461 manufacturer's instructions. For measurements a FACSCelesta SORP flow cytometer (BD Biosciences)
462 was employed, and data were evaluated with the LEGENDplex™ Data Analysis software.
463

464 **Production and purification of recombinant SARS-CoV-2 Spike proteins (see Figure 1-figure**
465 **supplement 1)**

466 SARS-CoV-2 Spike expression vectors were purchased from SinoBiological (see reagent table). Endotoxin-
467 free plasmids were prepared by Alta Biotech and provided at a concentration is 5mg/mL. Transfections
468 were carried out using CHO Freestyle cells (Invitrogen). 1.24mg of plasmid DNA was transfected into 90
469 million cells were using a MaxCyte Electroporation Transfection System. A detailed protocol is available

470 at https://maxcyte.com/atx. Culture supernatants were harvested on day 6 and clarified by centrifugation,
471 followed by filtration through a 0.45μm filter, followed by the addition of EDTA-free protease inhibitor
472 cocktail tablets (Roche). Culture supernatants were then dialyzed overnight at 4℃ in HBS (150mM NaCl,
473 10mM HEPES, pH 8.0) using 10kDa MWCO Slide-A-Lyzer dialysis cassettes (Thermo Scientific).
474 Supernatants were passed over a 10 ml StrepTrap HP column (Cytiva) at 1 ml/min using an ÄKTA pure
475 150 purifier (Cytiva), maintained at 4°C. Bound protein was eluted with elution buffer (2.5mM
476 desthiobiotin, 100mM Tris-Cl, 150mM NaCl, 1mM EDTA, pH 8.0). Peak fractions were pooled and
477 concentrated using 30kDa MW CO Amicon centrifugal concentrators (Millipore). Trace endotoxins were
478 removed by two sequential Triton X114 extractions, followed by passage through an HiPPR detergent
479 removal column (Thermo Fisher). Following the removal of endotoxin, the remaining contamination was
480 assessed using the Pierce™ Chromogenic Endotoxin Quant Kit (Thermo Fisher), based on the amebocyte
481 lysate assay. The endotoxin level in the purified recombinant protein preparation is below 1.0 EU/ml, which
482 closely aligns with the levels specified by the company for recombinant proteins. Protein concentrations
483 were determined by a BCA Protein assay (Thermo Fisher).
484

485 **Viral like particles and lentivirus preparation**

486 SARS-CoV-2 Spike protein incorporated NL4.3-GFP VLPs were produced by transfecting HEK293T cells
487 with full length SARS-CoV-2 Spike-S and HIV-1 NL4-3 Gag-iGFP ΔEnv (12455, NIH AIDS Reagent
488 Program) at a ratio of 1:2.5 using a previously reported method (32). EGFP control lentiviruses (no Spike
489 protein) were produced by transfecting HEK293T cells with pCMV-dR8.2 dvpr (packaging) and
490 pLentipuro3 TO V5-GW EGFP-Firefly Luciferase (reporter). Coronavirus Spike proteins were
491 incorporated by co-transfection with SARS-CoV-2 Spike-S, HCoV-229E Spike, or HCoV-HKU1 Spike
492 expressing plasmids. Eighty percent confluent HEK293T in six well plates (2.5 ml/well) were transfected
493 with 5 μg of plasmid diluted in Opti-MEM with a 1:4 (DNA/reagent) dilution of TransIT-293 Transfection
494 Reagent. The media was harvested 64 hr later and centrifuged at 500 ×g for 10 min at 4 °C. The supernatants
495 were collected and mixed with Lenti-X Concentrator (Takara Bio USA, Inc) at a 1:3 ratio. The mixture was
496 placed at 4 °C overnight and centrifuged the following day at 1500 ×g for 45 min. Fluorescent VLPs were
497 directly counted and measured by BD FACSCelesta™ flow cytometer. The forward scatter (FSC) detector
498 (Photodiode with 488/10 BP filter) and side scatter (SSC) detector (photomultiplier tube (PMT) with 488/10
499 BP filter) were tuned to detect voltages up to 530 for FSC and 220 for SSC. The NL4.3-GFP VLPs were
500 distinguished from noise and non-VLP particles by GFP signals. NL4.3-GFP VLP Spike protein
501 incorporation was tested using human ACE2 expressing HEK293 cells (ACE2/HEK293). Ten thousand
502 VLPs were incubated with 1×10^4 ACE2/HEK293 cells in 1× HBSS (contains; 1 mM Ca^{2+}, 2 mM Mg^{2+}, 1

503 mM Mn^{2+} and 0.5% fatty acid free BSA) buffer at 4 °C for 30 min. Binding of the VLPs to ACE2/HEK293
504 cells was measured with BD FACSCelesta™. The 50% lentivirus transduction dose was determined using
505 percentile (50%) of GFP positive ACE2/HEK293 cells 3 days after transduction. The pelleted VLPs or
506 lentiviruses were suspended in PBS and frozen in single use aliquots.
507

508 **Lentivirus transduction assay**

509 96-well plates were seeded with 200 µl of ACE2/HEK293 cells (1.5×10^4 cells/ml). After a 24 h incubation,
510 recombinant proteins or neutralizing antibody was added. Lentiviral particles capable of transducing 50%
511 of the cells (CoV2-lenti, HKU1-lenti, and 229E-lenti) were added (~25 µl) 30 min later. Following a three-
512 day culture, the ACE2/HEK293 cells were harvested and GFP expression levels determined by BD
513 FACSCelesta™ flow cytometry. Each group contained 2-5 replicates.
514

515 **Measurement of vascular permeability**

516 Pulmonary vascular permeability was measured by i.v. administration of Evans blue dye (0.2 ml 0.5% in
517 PBS) (50). One and half hours after Spike protein nasal administration, Evans blue dye was injected
518 intravenously. After another 1.5 hours the mice were perfused with PBS, and lungs and livers were
519 harvested, and dye extracted in formamide overnight at 55˚C. Dye concentrations were quantified by
520 measuring absorbance at 610 nm with subtraction of reference absorbance at 450 nm. The content of Evans
521 blue dye was determined by generating a standard curve from dye dilutions.
522

523 **NETosis assays**

524 Mouse bone marrow derived- or human neutrophils (> 97% purity) were resuspended in RPMI 1640 media
525 (1×10^6/ml) and incubated at 37°C in 5% CO_2 for 30 min. To induce NETosis, the cells were exposed to N-
526 formylmethionyl-leucyl-phenylalanine (fMLP, 1 µM); lipopolysaccharide (LPS, 10 ng/ml); tumor necrosis
527 factor-α (TNFα, 20 ng/ml); phorbol myristate acetate (PMA, 30 nM), or four different SARS-CoV Spike
528 protein preparations (0.1µg/ml or 1µg/ml) for 4 hours to overnight at 37℃. The cultures were terminated
529 by adding 4% PFA for 15 min. Helix NP™ NIR (0.1 µM; Biolegend) and DAPI (0.3 nM; Biolegend) were
530 added to detect NETs. Data acquisition (Helix NP™ NIR^+ $DAPI^+$ Cells) was done on FACSCelesta SORP
531 (BD) flow cytometer and analyzed with FlowJo software (Tree star). *In vitro* imaging of NETosis was
532 performed using a modified protocol from a previous report (51). The A549 cells were plated 48 hr before
533 imaging at 60% cell confluent. Fluorescently labeled SARS-CoV-2 Spike protein (Alexa Fluor 488; 0.5
534 µg/ml) was added to the A549 cells 24 hr before human neutrophil seeding. Human neutrophils were

purified from whole blood by EasySep™ Direct Human Neutrophil Isolation Kit (Stem cell). Purified human neutrophils were stained with Hoechst prior to seeding on SARS-CoV-2 Spike protein pre-treated A549 cells in Propidium Iodide (PI, 1 μg/ml) containing culture media. Time-lapse images were acquired with a Leica SP8 inverted 5 channels confocal microscope (Leica Microsystems) equipped with 40× oil objective, 0.95 NA (immersion medium used distilled water). The temperature of air (5% CO_2) was maintained at 37.0± 0.5°C. Time interval between frames were set as 10 min for 5 hr acquisition. The loss of nucleus of human neutrophils was detected by the loss of Hoechst signal and extracellular DNA released by NETosis was labeled by PI signals.

Fluorescent nanobead binding assay of SARS-CoV-2 Spike protein

FluoSpheres™ NeutrAvidin™-Labeled Microspheres, 0.2 μm, yellow-green fluorescent (505/515), 1% solids (Cat# F8774, Thermo Fisher Scientific Inc.) was used as a nanobead platform for SARS-CoV-2 Spike protein conjugation. Fluorescent nanobead were directly counted and measured by BD FACSCelesta™ flow cytometer. A flow cytometer equipped with forward scatter (FSC) detector (Photodiode with 488/10 BP filter) and side scatter (SSC) detector (photomultiplier tube (PMT) with 488/10 BP filter) was tuned to detect voltages up to 550 for FSC and 230 for SSC. Million counts of nanobeads were conjugated with 0.5 μg of SARS-CoV-2 Spike protein by interaction of Neutravidin on beads and Strep Tag II on recombinant proteins. Nanobeads and SARS-CoV-2 Spike proteins in PBS were coupled at room temperature for one hour and washed with 1 ml of PBS. Coupled nanobeads spun were down with benchtop centrifuge speed at 20,000 ×g, 4°C for 20 min. The nanobeads pellet was suspended with PBS concentration at 2×10^4/μl. SARS-CoV-2 Spike protein couplings to nanobeads were tested with Alexa Fluor 647 conjugated SARSCoV-2 Spike neutralizing antibody (Cat# 40591-MM45, SinoBiological). To test binding ability of various recombinant proteins (human ACE2, human Siglec-5, human Siglec-8, mouse ACE2, and mouse Siglec-F) were directly conjugated with Alexa Fluor 647. SARS-CoV-2 Spike protein conjugated nanobeads (2×10^4 counts) in 20 μl of 1× HBSS (contains; 1 mM Ca^{2+}, 2 mM Mg^{2+}, 1 mM Mn^{2+} and 0.5% fatty acid free BSA) buffer were incubated with 0.2 μg of fluorescent recombinant proteins at room temperature for 30 min. Fluorescent antibody or recombinant protein biding on fluorescent nanobeads were directly counted and measured by BD FACSCelesta™ flow cytometer.

Thick section immunohistochemistry and confocal microscopy

Immunohistochemistry was performed using a modified method of a previously published protocol (32, 52). Briefly, freshly isolated lungs were fixed in newly prepared 4% paraformaldehyde (Electron

567 Microscopy Science) overnight at 4 °C on an agitation stage. Fixed lungs were embedded in 4% low melting
568 agarose (Thermo Fisher Scientific) in PBS and sectioned with a vibratome (Leica VT-1000 S) at a 50 µm
569 thickness. Thick sections were blocked in PBS containing 10% fetal calf serum, 1 mg/ml anti-Fcγ receptor
570 (BD Biosciences), and 0.1% Triton X-100 (Sigma) for 30 min at room temperature. Sections were stained
571 overnight at 4°C on an agitation stage with Ly6G, Siglec-F, CD169, CD31, and F4/80, and labelled WGA.
572 Stained thick sections were microscopically analyzed using a Leica SP8 confocal microscope equipped
573 with an HC PL APO CS2 40× (NA, 1.30) oil objective (Leica Microsystem, Inc.) and images were
574 processed with Leica LAS AF software (Leica Microsystem, Inc.) and Imaris software v.9.9.1 64× (Oxford
575 Instruments plc). The intensities of fluorescent signals in regions of interests (ROI) were measured by LSA
576 AF Lite software (Leica Microsystem).
577

578 ***In vitro* imaging of HEK293 cells**

579 HEK293 cells were transfected using TransIT-293 transfection reagent (Mirus Bio LLC). For transient
580 expression of human Siglec-5-GFP 80% confluent HEK293 in 8 well chamber slide (0.25 ml/well) were
581 transfected by adding dropwise to each well 25 µl containing 0.25 µg of plasmid diluted in Opti-MEM with
582 a 1:4 (DNA/reagent) dilution of TransIT-293 Transfection Reagent. To generate a stable cell line of human
583 Siglec-5-GFP and human ACE2-OFP transfected HEK293 cells were sorted with FACS Aria II by GFP and
584 OFP signals. Sorted human Siglec-5-GFP transfected HEK293 cells were further selected with G418 (0.8
585 mg/ml) containing growth media and maintained with G418 (0.5 mg/ml) media. Sorted human ACE2OFP
586 transfected HEK293 cells were further selected with hygromycin B (0.2 mg/ml) containing growth media
587 and maintained with hygromycin B (0.1 mg/ml) media. Transiently transfected HEK293 cells in 8 well
588 chamber slide were directly imaged with a Leica SP8 inverted five channels confocal microscope (Leica
589 Microsystems). HEK293 cells, HEK293 Siglec-5-GFP, and HEK293 ACE2-OFP cell lines were plated at a
590 ratio of 1:1:1 (cell numbers) in 8 well chamber with normal media 18 hr prior to imaging. Imaging was
591 performed with a confocal microscope equipped with 40 × oil objective, 0.95 NA (immersion medium used
592 distilled water). The temperature of air (5% CO_2) was maintained at 37.0 ± 0.5°C. Fluorescent SARS-CoV-
593 2 Spike protein (Alexa Fluor 647) (1 µg/ml) was added into culture media. Images were acquired with Leica
594 LAS AF software (Leica Microsystem, Inc) and processed with Imaris software v.9.9.1 64× (Oxford
595 Instruments plc).
596

597 **Time-lapse imaging of lung sections with confocal microscopy**

598 Lung slices were obtained from mouse lungs using a slightly modified published protocol (53). Briefly,
599 C57BL/6 mice were euthanized with overdose of Avertin (1 ml of 2.5% Avertin). The peritoneum was

600 opened, and the descending aorta cut allowing blood to pool in the abdomen. The trachea was cannulated,
601 and the lungs inflated with 37 °C 1.5% low-melting-point agarose (Cat# 50111, Lonza) prepared with RPMI
602 1640 media. Subsequently, the lungs were excised and rinsed with RPMI 1640 media. Isolated left lungs
603 were sectioned into six to eight 1-mm-thick transverse slices using a #10 scalpel blade. Lung slices were
604 placed in a pre-warmed cover glass chamber slide (Nalgene, Nunc) under a metal flat washer (M8- 5/16th
605 inches diameter). The chamber slide was then placed into the temperature control chamber on the
606 microscope. The temperature of air was monitored and maintained at 37.0± 0.5°C for 5% CO_2. Mounted
607 lung sections on the chamber slide were microscopically analyzed using a Leica SP8 confocal microscope
608 equipped with an HC PL APO CS2 40× (NA, 1.30) oil objective (Leica Microsystem, Inc.) and images
609 were processed with Leica LAS AF software (Leica Microsystem, Inc.). Lung slices were imaged a range
610 of depths (10-50 μm). Time-lapse images were processed with Imaris software v.9.9.1 64× (Oxford
611 Instruments plc).
612

613 **Intravital imaging**

614 The microanatomy of liver, spleen, heart, Peyer's patch, and inguinal LN were delineated by tail vein
615 injection of labelled antibodies before imaging. Antibodies used included CD31, blood vessels; F4/80,
616 Kupffer cells and macrophages; CD169, subcapsular macrophages; and Ly6G; neutrophils). The antibody
617 mixtures were injected 10 min before starting animal surgery. Fluorescently labelled Spike proteins were
618 injected intravenously or at the mouse tail base as indicated. To image the liver or spleen a slightly modified
619 published protocol was used (54). Briefly, after initial anesthesia (Avertin 300 mg/kg, i.p.) the skin and
620 peritoneum were cut to expose the left lobe of the liver, or the left flank was cut below the costal margin to
621 expose the spleen. The visible organs were glued with n-butyl cyanoacrylate to a custom-made metal holder.
622 After attachment, the mouse was placed over a pre-warmed cover glass (Brain Research Laboratories)
623 window on universal mounting frame AK-Set (PECON®). The exposed organs were kept moist with saline
624 wetted gauze. The mounting frame was placed into the temperature control chamber on the microscope and
625 maintained at 37.0± 0.5°C. Once stabilized onto imaging stage/insert the mice received isoflurane (Baxter;
626 2% for induction of anesthesia, and 1 – 1.5% for maintenance, vaporized in an 80:20 mixture of oxygen
627 and air). For liver and spleen four-dimensional analysis of cell behavior, stacks of various numbers of
628 section (z step = 3, 5) were acquired every 5-30 sec to provide an imaging volume of 20 ~ 50 μm in depth.
629 Intact organ imaging of the heart, inguinal lymph node, or Peyer's patches was performed after mouse
630 sacrifice using same imaging procedure as used for liver/spleen imaging.
631 To image neutrophils in the cremaster muscle (31), mice received an intrascrotal injection of PBS,
632 BSA, IL-1β (50 ng in 300 μl saline, R&D Systems), Spike proteins, or IL-1b and Spike proteins. 90 min.

633 prior to imaging, the mice received injections of Avertin (300 mg/kg, i.p.) and fluorescently labeled
634 antibodies intravenously. Antibodies used directed against Gr-1, neutrophils; GPIbβ, platelets; and CD31,
635 blood vessel endothelium. The isolated cremaster tissue was exteriorized and stabilized onto the imaging
636 stage/insert with the tissue directly contacting the cover glass. The exposed tissue was kept moist with
637 prewarmed saline (37°C). Once stabilized onto an imaging stage/insert the mouse received isoflurane
638 (Baxter; 2% for induction of anesthesia, and 1 – 1.5% for maintenance, vaporized in an 80:20 mixture of
639 oxygen and air), and placed into a temperature-controlled chamber. Image stacks of optical sections (z
640 step=1) were routinely acquired at 20 – 30 sec intervals to provide an imaging volume of 15-25 µm. All
641 imaging was performed with a Leica SP8 inverted 5 channels confocal microscope (Leica Microsystems)
642 equipped with HC PL APO CS2 40× (NA, 1.30) oil objective. Sequences of image stacks were transformed
643 into volume-rendered four-dimensional videos using Imaris software v.9.9.1 64x (Oxford Instruments plc).
644 Video editing was performed using Adobe Premiere Pro 2022 (Adobe Systems Incorporated).
645

646 **Quantifications and Statistical Analyses**

647 All experiments were performed at least three times. Representative images were placed in figures. Primary
648 image data which was analyzed and calculated by Leica LAS AF software (Leica Microsystem, Inc.) or
649 Imaris software v.9.9.1 64× (Oxford Instruments plc). was acquired and processed with Microsoft Excel
650 software. Error bars with ±SEM, and p values were calculated with unpaired t-test in GraphPad Prism 9.3.1
651 (GraphPad software). $p<0.05$ was considered significantly different.
652

653 **REFERENCES**

654

655 1. Zhou P, Yang XL, Wang XG, Hu B, Zhang L, Zhang W, et al. A pneumonia outbreak associated
656 with a new coronavirus of probable bat origin. Nature. 2020;579(7798):270-3.
657 2. Wrapp D, Wang N, Corbett KS, Goldsmith JA, Hsieh CL, Abiona O, et al. Cryo-EM structure of
658 the 2019-nCoV spike in the prefusion conformation. Science. 2020;367(6483):1260-3.
659 3. Fan X, Cao D, Kong L, Zhang X. Cryo-EM analysis of the post-fusion structure of the SARS-CoV
660 spike glycoprotein. Nat Commun. 2020;11(1):3618.
661 4. Ke Z, Oton J, Qu K, Cortese M, Zila V, McKeane L, et al. Structures and distributions of
662 SARSCoV-2 spike proteins on intact virions. Nature. 2020;588(7838):498-502.
663 5. Lan J, Ge J, Yu J, Shan S, Zhou H, Fan S, et al. Structure of the SARS-CoV-2 spike receptorbinding
664 domain bound to the ACE2 receptor. Nature. 2020;581(7807):215-20.

665 6. Benton DJ, Wrobel AG, Xu P, Roustan C, Martin SR, Rosenthal PB, et al. Receptor binding and
666 priming of the spike protein of SARS-CoV-2 for membrane fusion. Nature. 2020;588(7837):327-30.
667 7. Li F, Li W, Farzan M, Harrison SC. Structure of SARS coronavirus spike receptor-binding domain
668 complexed with receptor. Science. 2005;309(5742):1864-8.
669 8. Ou X, Liu Y, Lei X, Li P, Mi D, Ren L, et al. Characterization of spike glycoprotein of SARSCoV-
670 2 on virus entry and its immune cross-reactivity with SARS-CoV. Nat Commun. 2020;11(1):1620.
671 9. Shang J, Wan Y, Luo C, Ye G, Geng Q, Auerbach A, et al. Cell entry mechanisms of SARS-CoV-
672 2. Proc Natl Acad Sci U S A. 2020;117(21):11727-34.
673 10. Shang J, Ye G, Shi K, Wan Y, Luo C, Aihara H, et al. Structural basis of receptor recognition by
674 SARS-CoV-2. Nature. 2020;581(7807):221-4.
675 11. Yan R, Zhang Y, Li Y, Xia L, Guo Y, Zhou Q. Structural basis for the recognition of SARS-CoV2
676 by full-length human ACE2. Science. 2020;367(6485):1444-8.
677 12. Lenza MP, Oyenarte I, Diercks T, Quintana JI, Gimeno A, Coelho H, et al. Structural
678 Characterization of N-Linked Glycans in the Receptor Binding Domain of the SARS-CoV-2 Spike Protein
679 and their Interactions with Human Lectins. Angew Chem Int Ed Engl. 2020;59(52):23763-71.
680 13. Walls AC, Tortorici MA, Frenz B, Snijder J, Li W, Rey FA, et al. Glycan shield and epitope masking
681 of a coronavirus spike protein observed by cryo-electron microscopy. Nat Struct Mol Biol.
682 2016;23(10):899-905.
683 14. Yang Q, Hughes TA, Kelkar A, Yu X, Cheng K, Park S, et al. Inhibition of SARS-CoV-2 viral entry
684 upon blocking N- and O-glycan elaboration. Elife. 2020;9.
685 15. Hoffmann M, Kleine-Weber H, Schroeder S, Kruger N, Herrler T, Erichsen S, et al. SARS-CoV-2
686 Cell Entry Depends on ACE2 and TMPRSS2 and Is Blocked by a Clinically Proven Protease Inhibitor.
687 Cell. 2020;181(2):271-80 e8.
688 16. Hoffmann M, Kleine-Weber H, Pohlmann S. A Multibasic Cleavage Site in the Spike Protein of
689 SARS-CoV-2 Is Essential for Infection of Human Lung Cells. Mol Cell. 2020;78(4):779-84 e5.
690 17. Takeda M. Proteolytic activation of SARS-CoV-2 spike protein. Microbiol Immunol.
691 2022;66(1):15-23.
692 18. Errico JM, Adams LJ, Fremont DH. Antibody-mediated immunity to SARS-CoV-2 spike. Adv
693 Immunol. 2022;154:1-69.
694 19. Troyer Z, Alhusaini N, Tabler CO, Sweet T, de Carvalho KIL, Schlatzer DM, et al. Extracellular
695 vesicles carry SARS-CoV-2 spike protein and serve as decoys for neutralizing antibodies. J Extracell
696 Vesicles. 2021;10(8):e12112.
697 20. Swank Z, Senussi Y, Manickas-Hill Z, Yu XG, Li JZ, Alter G, et al. Persistent circulating
698 SARSCoV-2 spike is associated with post-acute COVID-19 sequelae. Clin Infect Dis. 2022.

699 21. Theoharides TC. Could SARS-CoV-2 Spike Protein Be Responsible for Long-COVID Syndrome?
700 Mol Neurobiol. 2022;59(3):1850-61.
701 22. Thanh Le T, Andreadakis Z, Kumar A, Gomez Roman R, Tollefsen S, Saville M, et al. The
702 COVID19 vaccine development landscape. Nat Rev Drug Discov. 2020;19(5):305-6.
703 23. Lamprinou M, Sachinidis A, Stamoula E, Vavilis T, Papazisis G. COVID-19 vaccines adverse
704 events: potential molecular mechanisms. Immunol Res. 2023:1-17.
705 24. Hsieh CL, Goldsmith JA, Schaub JM, DiVenere AM, Kuo HC, Javanmardi K, et al. Structurebased
706 design of prefusion-stabilized SARS-CoV-2 spikes. Science. 2020;369(6510):1501-5.
707 25. Yurkovetskiy L, Wang X, Pascal KE, Tomkins-Tinch C, Nyalile TP, Wang Y, et al. Structural and
708 Functional Analysis of the D614G SARS-CoV-2 Spike Protein Variant. Cell. 2020;183(3):739-51 e8.
709 26. Zhang L, Jackson CB, Mou H, Ojha A, Peng H, Quinlan BD, et al. SARS-CoV-2 spike-protein
710 D614G mutation increases virion spike density and infectivity. Nat Commun. 2020;11(1):6013.
711 27. Volz E, Hill V, McCrone JT, Price A, Jorgensen D, O'Toole A, et al. Evaluating the Effects of SARS-
712 CoV-2 Spike Mutation D614G on Transmissibility and Pathogenicity. Cell. 2021;184(1):64-75 e11. 28.
713 Aida Y, Pabst MJ. Removal of endotoxin from protein solutions by phase separation using Triton X-114. J
714 Immunol Methods. 1990;132(2):191-5.
715 29. Hetzel M, Ackermann M, Lachmann N. Beyond "Big Eaters": The Versatile Role of Alveolar
716 Macrophages in Health and Disease. Int J Mol Sci. 2021;22(7).
717 30. Matthew CB, Sils IV, Bastille AM. Tissue-specific extravasation of albumin-bound Evans blue in
718 hypothermic and rewarmed rats. Can J Physiol Pharmacol. 2002;80(3):233-43.
719 31. Yan SL, Hwang IY, Kamenyeva O, Kabat J, Kim JS, Park C, et al. Unrestrained Galpha(i2)
720 Signaling Disrupts Neutrophil Trafficking, Aging, and Clearance. Front Immunol. 2021;12:679856.
721 32. Park C, Arthos J, Cicala C, Kehrl JH. The HIV-1 envelope protein gp120 is captured and displayed
722 for B cell recognition by SIGN-R1(+) lymph node macrophages. Elife. 2015;4.
723 33. Youn YJ, Lee YB, Kim SH, Jin HK, Bae JS, Hong CW. Nucleocapsid and Spike Proteins of
724 SARSCoV-2 Drive Neutrophil Extracellular Trap Formation. Immune Netw. 2021;21(2):e16.
725 34. Perez-Zsolt D, Erkizia I, Pino M, Garcia-Gallo M, Martin MT, Benet S, et al. Anti-Siglec-1
726 antibodies block Ebola viral uptake and decrease cytoplasmic viral entry. Nat Microbiol. 2019;4(9):155870.
727 35. Perez-Zsolt D, Munoz-Basagoiti J, Rodon J, Elosua-Bayes M, Raich-Regue D, Risco C, et al.
728 SARS-CoV-2 interaction with Siglec-1 mediates trans-infection by dendritic cells. Cell Mol Immunol.
729 2021;18(12):2676-8.
730 36. Hammonds JE, Beeman N, Ding L, Takushi S, Francis AC, Wang JJ, et al. Siglec-1 initiates
731 formation of the virus-containing compartment and enhances macrophage-to-T cell transmission of HIV1.
732 PLoS Pathog. 2017;13(1):e1006181.

733 37. Connolly NP, Jones M, Watt SM. Human Siglec-5: tissue distribution, novel isoforms and domain
734 specificities for sialic acid-dependent ligand interactions. Br J Haematol. 2002;119(1):221-38.
735 38. Sefik E, Qu R, Junqueira C, Kaffe E, Mirza H, Zhao J, et al. Inflammasome activation in infected
736 macrophages drives COVID-19 pathology. Nature. 2022;606(7914):585-93.
737 39. Vora SM, Lieberman J, Wu H. Inflammasome activation at the crux of severe COVID-19. Nat Rev
738 Immunol. 2021;21(11):694-703.
739 40. Aizawa H, Zimmermann N, Carrigan PE, Lee JJ, Rothenberg ME, Bochner BS. Molecular analysis
740 of human Siglec-8 orthologs relevant to mouse eosinophils: identification of mouse orthologs of Siglec-5
741 (mSiglec-F) and Siglec-10 (mSiglec-G). Genomics. 2003;82(5):521-30.
742 41. Tsai CM, Riestra AM, Ali SR, Fong JJ, Liu JZ, Hughes G, et al. Siglec-14 Enhances
743 NLRP3Inflammasome Activation in Macrophages. J Innate Immun. 2020;12(4):333-43.
744 42. Honzke K, Obermayer B, Mache C, Fathykova D, Kessler M, Dokel S, et al. Human lungs show
745 limited permissiveness for SARS-CoV-2 due to scarce ACE2 levels but virus-induced expansion of
746 inflammatory macrophages. Eur Respir J. 2022;60(6).
747 43. Lu Q, Liu J, Zhao S, Gomez Castro MF, Laurent-Rolle M, Dong J, et al. SARS-CoV-2 exacerbates
748 proinflammatory responses in myeloid cells through C-type lectin receptors and Tweety family member 2.
749 Immunity. 2021;54(6):1304-19 e9.
750 44. Sun W, Wu W, Jiang N, Ge X, Zhang Y, Han J, et al. Highly Pathogenic PRRSV-Infected Alveolar
751 Macrophages Impair the Function of Pulmonary Microvascular Endothelial Cells. Viruses. 2022;14(3).
752 45. Bernard I, Limonta D, Mahal LK, Hobman TC. Endothelium Infection and Dysregulation by
753 SARS-CoV-2: Evidence and Caveats in COVID-19. Viruses. 2020;13(1).
754 46. Nader D, Kerrigan SW. Molecular Cross-Talk between Integrins and Cadherins Leads to a Loss of
755 Vascular Barrier Integrity during SARS-CoV-2 Infection. Viruses. 2022;14(5).
756 47. Dominguez-Soto A, Aragoneses-Fenoll L, Gomez-Aguado F, Corcuera MT, Claria J,
757 GarciaMonzon C, et al. The pathogen receptor liver and lymph node sinusoidal endotelial cell C-type lectin
758 is expressed in human Kupffer cells and regulated by PU.1. Hepatology. 2009;49(1):287-96.
759 48. Kondo Y, Larabee JL, Gao L, Shi H, Shao B, Hoover CM, et al. L-SIGN is a receptor on liver
760 sinusoidal endothelial cells for SARS-CoV-2 virus. JCI Insight. 2021;6(14).
761 49. Sung PS, Yang SP, Peng YC, Sun CP, Tao MH, Hsieh SL. CLEC5A and TLR2 are critical in SARS-
762 CoV-2-induced NET formation and lung inflammation. J Biomed Sci. 2022;29(1):52.
763 50. Zhou Y, Schneider DJ, Morschl E, Song L, Pedroza M, Karmouty-Quintana H, et al. Distinct roles
764 for the A2B adenosine receptor in acute and chronic stages of bleomycin-induced lung injury. J Immunol.
765 2011;186(2):1097-106.

766 51. Hoppenbrouwers T, Autar ASA, Sultan AR, Abraham TE, van Cappellen WA, Houtsmuller AB, et
767 al. In vitro induction of NETosis: Comprehensive live imaging comparison and systematic review. PLoS
768 One. 2017;12(5):e0176472.
769 52. Park C, Hwang IY, Kehrl JH. The Use of Intravital Two-Photon and Thick Section Confocal
770 Imaging to Analyze B Lymphocyte Trafficking in Lymph Nodes and Spleen. Methods Mol Biol.
771 2018;1707:193-205.
772 53. Pieretti AC, Ahmed AM, Roberts JD, Jr., Kelleher CM. A novel in vitro model to study
773 alveologenesis. Am J Respir Cell Mol Biol. 2014;50(2):459-69.
774 54. Matsumoto S, Kikuta J, Ishii M. Intravital Imaging of Liver Cell Dynamics. Methods Mol Biol.
775 2018;1763:137-43.

776

777 **Acknowledgements**: The authors thank Dr. Anthony Fauci for long standing encouragement**.**

778 **Funding:** This work was supported by Intramural Research Program of National Institute of Allergy and
779 Infectious Diseases.

780

781 **Author Contribution:** CP performed most of the mouse work; IYH performed the flow cytometry and
782 macrophage cytokine production; SLY performed the cremaster imaging, SV, DW, and DVR purified the
783 recombinant proteins, CC and JA supervised the protein purification and provided helpful advice, JHK
784 wrote the manuscript and oversaw the project.

785

786 **Competing interests:** The authors declare they have no competing interests. The content is solely the
787 responsibility of the authors and does not necessarily represent the official views of the National Institutes
788 of Health

789

790 **Data and Material Availability:** The primary imaging files are available from the corresponding author.

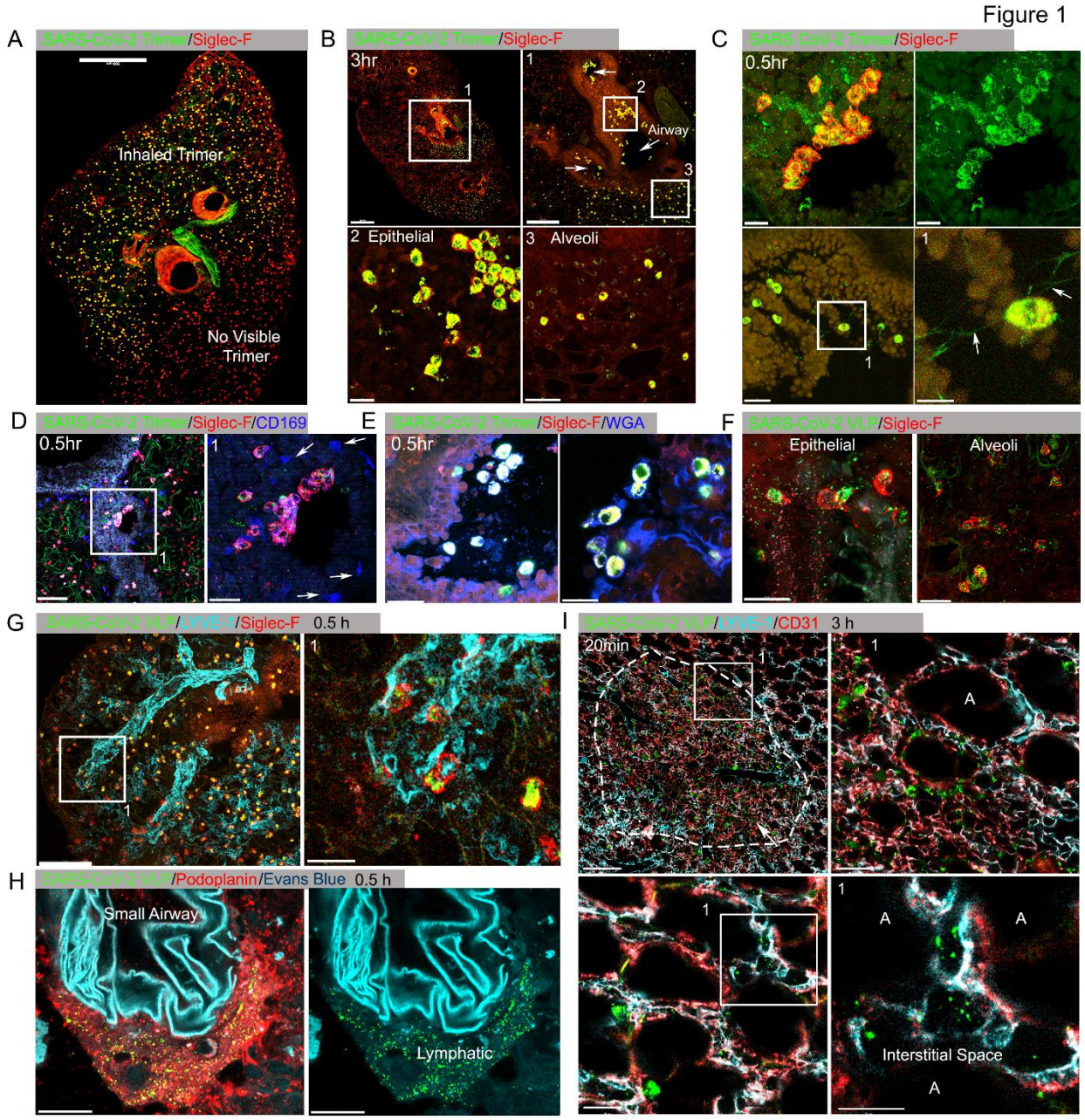

Figure 1. Lung images following intranasal administered SARS-CoV-2 Spike protein. **(A)** Confocal micrograph of a lung section 18 hr post SARS-CoV-2 Spike protein (Trimer) instillation. Alveolar macrophages (AMs) visualized with Siglec-F antibody. Alexa Fluor 488 conjugated recombinant SARS-CoV-2 Spike protein (3 µg in 50 µl of saline) was inoculated by nasal instillation. Spike-reached lung region (Instilled Trimer) and non-reached area (No visible Trimer) noted on the micrograph. Scale bar, 500 µm. **(B)** Confocal micrographs of lung collected at 3 hr post Spike protein instillation. AMs in the large airway and alveoli (upper left) area is shown. ROI-1 (box1) (upper right) is enlarged, and arrows indicate large

airways. ROI-2 (Box 2) (lower left) shows AMs bearing SARS-CoV-2 Spike protein on airway epithelial cells. ROI-3 (Box 3) (lower left) shows Spike protein bearing AMs in alveoli. Scale bars, 500, 200, 20, and 50 μm. (**C**) Confocal micrographs of lung collected at 0.5 hr post SARS-CoV-2 Spike protein instillation. AMs were visualized with Siglec-F antibody (upper left & right). AMs connected to each other (lower left) via tunneling nanotubes (arrows) (lower right). Scale bars, 20, 20, 30, and 10 μm. **(D & E)** Confocal micrographs of lung collected at 0.5 hr post Spike instillation. SARS-CoV-2 Spike protein (green) on airway epithelium and CD169$^+$ macrophages (D). Arrows indicate CD169$^+$ macrophages (right). Scale bars, 100 and 30 μm. AMs with SARS-CoV-2 Spike protein and Mucin (Alexa Fluor 647 conjugated wheat germ agglutin, WGA) on airway epithelium (E). Scale bars, 30 and 20 μm. **(F)** Confocal micrographs of lung collected at 2 hr post SARS-CoV-2 Spike protein incorporated VLP instillation (green). AMs (red, SiglecF) on epithelium (left) and in alveoli (right). Scale bars, 20 μm. **(G)** Confocal micrographs of lung collected at 0.5 hr post SARS-CoV-2 Spike VLP (green) instillation. AMs (red, Siglec-F antibody) and lung vasculatures visualized LYVE-1 (cyan) (top, left). LYVE-1$^+$ vasculature associated AMs bearing VLPs is highlighted (box) and enlarged (top, right). Scale bars, 100 and 25 μm. **(H)** A confocal micrograph shows a lung lymphatic vasculature visualized with Podoplanin antibody. Fifty microliters of a mixture of Evans blue (cyan) (5 μg) and Spike bearing VLPs (green) (0.5 million counts) were applied to the mouse nose. VLPs in lymphatics associated with a small airway highlighted (right). Scale bars, 20 μm. **(I)** Confocal micrographs of lung collected 20 min post Spike incorporated VLP (green) instillation. Lung vasculatures visualized CD31 (red) and LYVE-1 (cyan). Damaged lung tissue is indicated (dotted line) (upper left). Border of damaged tissue and intact alveoli (box) is enlarged (upper right). A lymphatic structure was stained by LYVE-1 in intact alveolus is highlighted (lower left). An image of VLPs in LYVE-1$^+$ lymphatic portal in alveoli (box) is enlarged (lower right). “A” indicates alveolus. Scale bars, 100, 20, 25, and 10 μm.

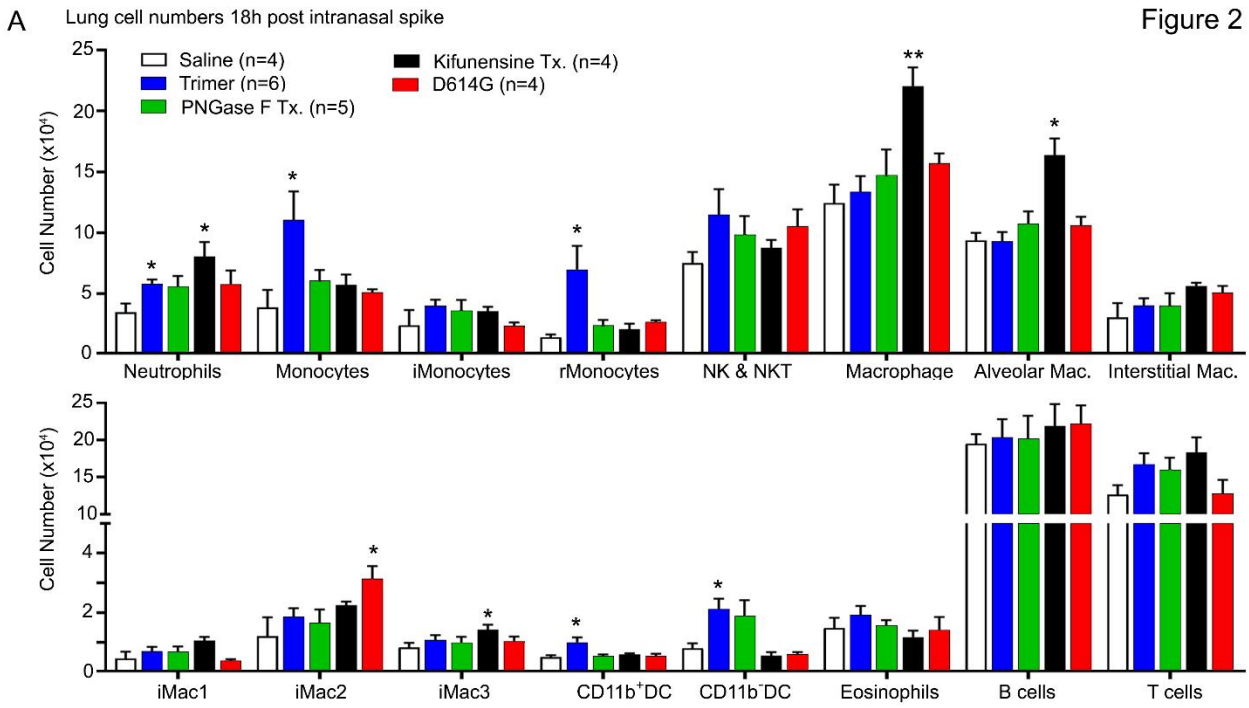

B Lung cell uptake at 18h post intranasal spike

Cell Type	Background	Percentage			
		Trimer (n=6)	PNGase F Tx. (n=5)	Kifunensine Tx. (n=8)	D614G (n=4)
Neutrophils	1.245 ± 0.149	3.395 ± 0.916	2.604 ± 0.998	2.084 ± 0.421	4.645 ± 1.484
rMono	1.130 ± 0.450	2.888 ± 0.759	1.204 ± 0.419	0.684 ± 0.095	6.983 ± 1.168 **
iMono	1.033 ± 0.159	3.565 ± 0.805	1.92 ± 0.701	0.856 ± 0.175 *	4.700 ± 0.669
AMac	1.025 ± 0.376	77.467 ± 5.924	62.906 ± 16.825 **	39.025 ± 5.412 ****	84.325 ± 1.674
iMac1	2.980 ± 0.720	9.288 ± 3.234	3.102 ± 1.242	2.754 ± 0.368	9.533 ± 1.162
iMac2	1.408 ± 0.098	13.583 ± 3.234	5.386 ± 1.250 *	2.093 ± 0.187 ***	8.870 ± 1.811
iMac3	1.755 ± 0.769	31.800 ± 7.223	36.642 ± 13.330	18.403 ± 5.740****	10.420 ± 2.022****
Eosinophils	1.438 ± 0.092	2.008 ± 0.539	1.758 ± 0.344	1.736 ± 0.272	5.125 ± 0.428 *
CD11b+DC	2.225 ± 0.597	5.962 ± 1.136	4.898 ± 1.004	7.383 ± 2.163	9.275 ± 1.126 *
CD11b-DC	2.240 ± 0.251	3.702 ± 0.633	5.372 ± 1.056	3.644 ± 0.477	7.143 ± 1.422 *
NK&NKT	0.658 ± 0.244	1.110 ± 0.176	1.014 ± 0.363	0.469 ± 0.100	3.688 ± 0.526
B	0.328 ± 0.099	1.055 ± 0.196	0.906 ± 0.293	0.386 ± 0.099	2.160 ± 0.264
T	0.156 ± 0.068	1.015 ± 0.360	0.432 ± 0.149	0.200 ± 0.027	2.338 ± 0.468

Figure 2. Lung leukocyte profile following intranasal administration of SARS-CoV-2 Spike proteins. **(A)** Leukocyte numbers in isolated lung tissue. Eighteen hr post intranasal administration of indicated Spike proteins lung tissue collected, processed, and leukocyte cell numbers determined by flow cytometry. Numbers of mice analyzed are indicated. Data mean +/- SEM, *$p < 0.05$; **$p < 0.005$. **(B)** SARS-CoV-2 Spike protein uptake by lung leukocytes 18 hr following intranasal inoculation. Flow cytometry results from indicated mice. Values significantly different from the WT SARS-CoV-2 protein (Trimer) are indicated, *$p < 0.05$; **$p < 0.01$; ***$p < 0.005$. ****$p<0.001$.

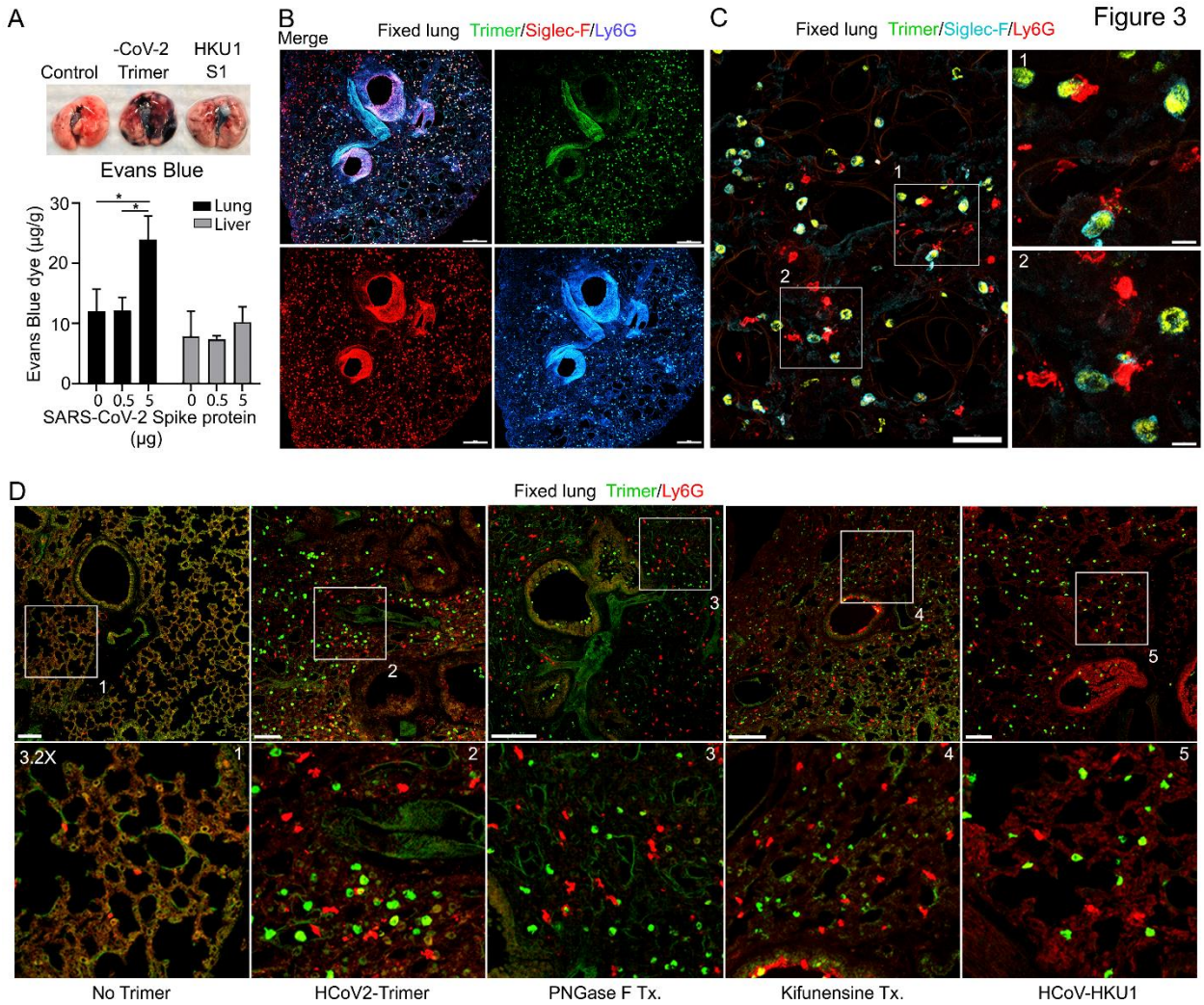

Figure 3. Increased lung vascular permeability and neutrophil localization following intranasal SARS-CoV-2 Spike protein. **(A)** Tissue photographs of lungs collected 2.5 hr post Spike protein (-CoV-2 Trimer), the S1 subunit of the human coronavirus (HKU1 S1), or saline instillation. Evans blue (200 ul of 5 mg/ml, PBS) was injected i.v. 1.5 hr post intranasal Spike administration. Lungs collected 1 hr after Evans blue injection. Evans blue amounts in lung and liver tissue are shown. **(B)** Confocal micrographs of lung collected at 18 hr post Spike protein. AMs and neutrophils detected with Siglec-F and Ly6G antibodies, respectively. Scale bar, 500 µm. **(C)** Confocal micrographs of lung collected at 3 hr post SARS-CoV-2 Spike protein instillation show SARS-CoV-2 Spike protein (green), neutrophils (red), and AMs (cyan). ROI-1 and -2 (boxes), show contact between AMs and neutrophils and are enlarged in the right panels. Scale bars, 50 and 10 µm. **(D)** Confocal micrographs of lung collected at 3 hr post each SARS-CoV-2 Spike proteins instillation show SARS-CoV-2 Spike protein (green) and neutrophils (red). From left to right of panels show saline (No Trimer), SARS-CoV-2 Spike protein (HCoV-2-Trimer), PNGase F treated SARS-CoV-2 Spike protein (PNGase F Tx.), SARS-CoV-2 Spike protein purified from Kifunensine treated cells

841 (Kifunensine Tx.), and the S1 subunit of the human coronavirus HKU1 (HCoV-HKU1) Spike Protein. ROIs
842 in each upper panel (boxes) are enlarged (3.2× magnification) in lower panels. Scale bars, 200 μm. *$p <$
843 0.05.

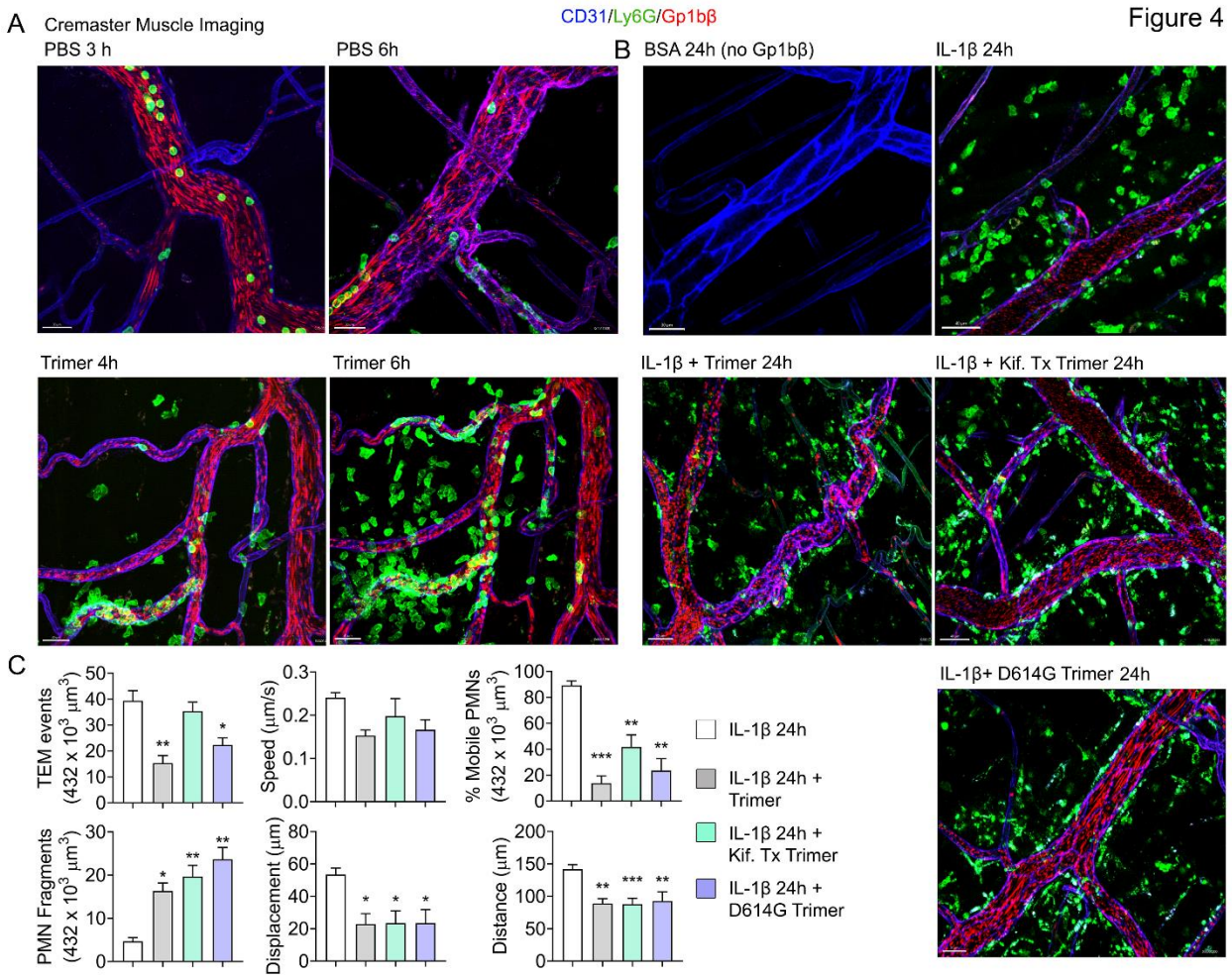

Figure 4. Mouse neutrophil damage following intrascrotal injections of Spike proteins. **(A & B)** Confocal snapshots of time-lapse movie of blood vessels in the cremaster muscle following PBS, BSA, Spike protein preparations (Trimer), IL-1β, or IL-1β plus Spike protein (5 μg) at indicated time points. Fluorescently labelled CD31, Ly6G, and Gp1bβ outlined the blood vessel endothelium, neutrophils, and platelets, respectively. Scale bars, 30 μm, except far right top and middle panels, 40 μm **(C)** Analysis of imaging data. The number of transendothelial migration (TEM) events recorded, neutrophil (PMN) fragments, and % mobile neutrophils in a defined imaging space over 20 min. Results of neutrophil tracking in the same defined volume including speed, displacement, and distance. Imaris software used for the tracking. *$p < 0.05$; **$p < 0.005$.

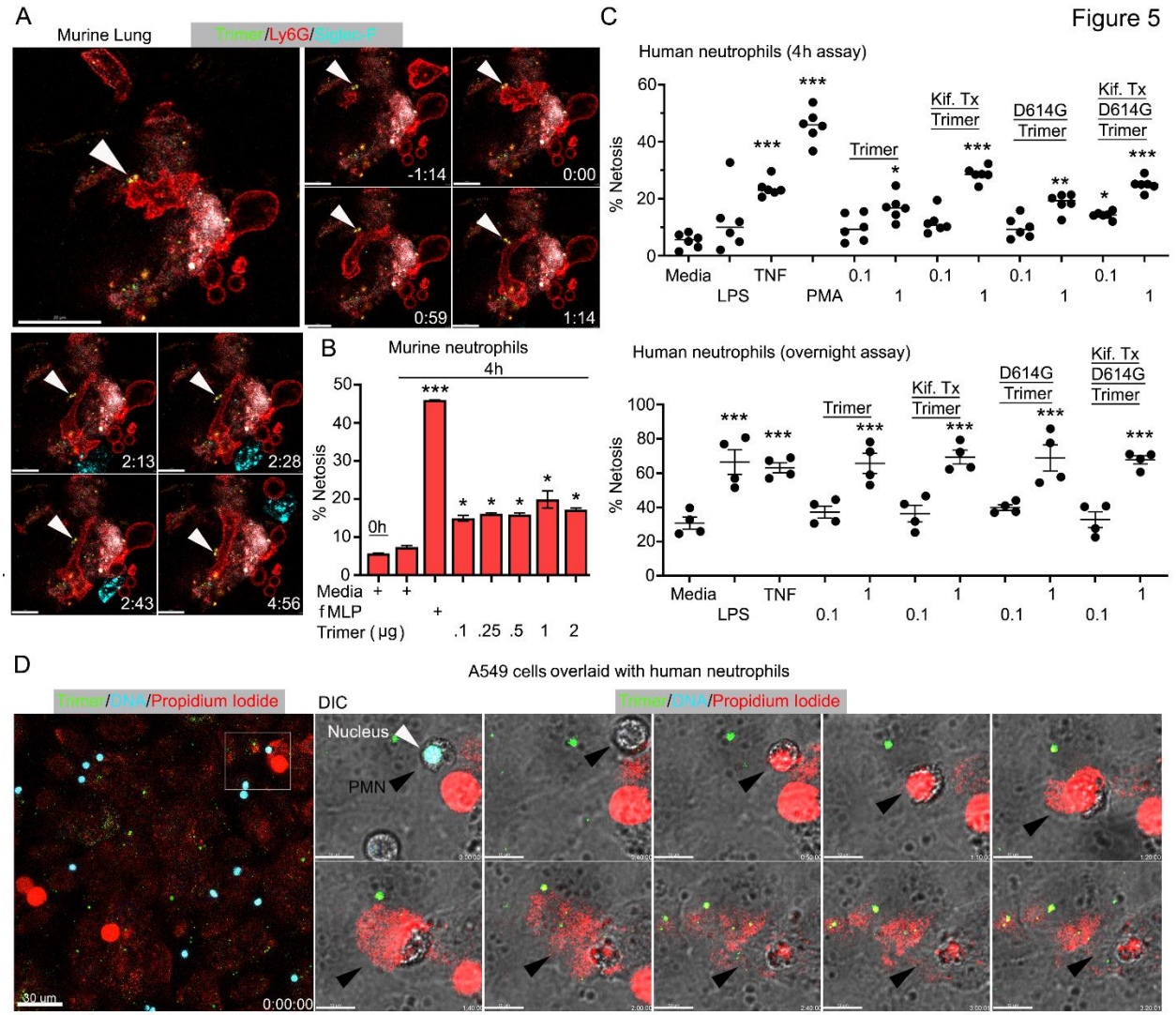

Figure 5. Neutrophil injury following exposure to SARS-CoV-2 Spike proteins. **(A)** Time-lapse images of a freshly sliced lung section 3 hr after SARS-CoV-2 Spike protein instillation. Neutrophils (Ly6G) and AMs (Siglec-F) were visualized by injected fluorescently tagged antibodies. Serial images show neutrophil behavior on Spike protein (Trimer) bearing cells. Arrowheads indicate Spike protein deposition. The time banner is set to 0:00 as neutrophil contacts Spike protein. Scale bars, 100, 25, and 20 µm. **(B)** Purified murine bone marrow neutrophils were exposed to increasing concentrations of Spike protein or fMLP (N-formyl-methionyl-leucyl-phenylalanine) for 4 hours or not. The percentage of neutrophils undergoing NETosis was measured by flow cytometry. **(C)** Purified human peripheral blood neutrophils were exposed to various Spike protein preparations, lipopolysaccharide (LPS), tumor necrosis factor-α (TNF) or phorbol myristate acetate (PMA). Graphs show the percentage of DAPI^{+}Helix NP NIR^{+} cells after either 4 hr or overnight culture. Each point represents a different donor. **(D)** A still image of *in vitro* time-lapse movie shows exposed neutrophil DNA (red, propidium iodide), neutrophil nucleus (cyan, Hoechst), and SARS-

865 CoV-2 Spike protein (trimer, green) bearing A549 cells. Plated A549 cells were treated with Spike protein
866 (0.5 μg/ml) 24 hr prior to Hoechst-stained human neutrophil seeding. Propidium iodide (1 μg/ml) was added
867 to the culture media and time-lapse images acquired every 10 min for 5 hr. Sequential DIC images overlay
868 with fluorescent images show neutrophil NETosis. White arrowhead indicates a neutrophil's intact nucleus
869 (cyan, Hoechst). Black arrowheads delineate a neutrophil undergoing NETosis as detected by exposed DNA
870 (red). Scale bars, 30 and 10 μm. *$p < 0.05$; **$p < 0.01$; ***$p < 0.005$.

871

872

873

874

875

876

877

878

879

880

881

882

883

884

885

886

887

888

889

A

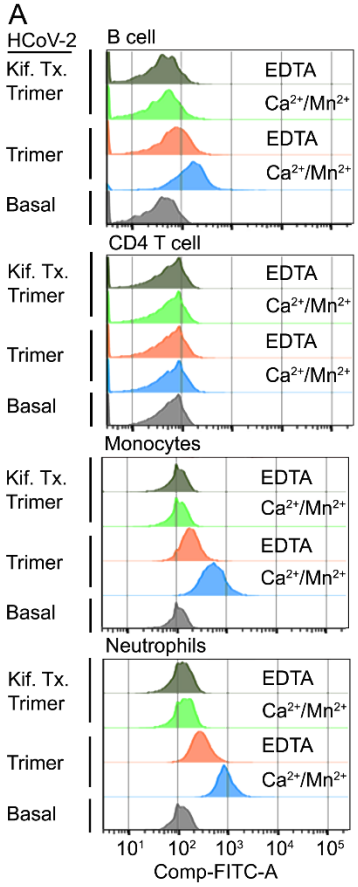

B

Figure 6

Cell Type	Buffer	HKU-1 S1 (N=2)	HCoV-2 S1 (N=4)	HCoV-2 (N=8)	Kif. Tx. (N=4)	D614G (N=3)
B cells	Mn^{2+}/Ca^{2+}	0.87+/-0.15	26.54+/-8.17	47.86+/-8.76	8.24+/-3.99	52.15+/-15.72
	EDTA	0.45+/-0.55	10.70+/-3.76	18.39+/-5.89	1.29+/-0.30	24.85+/-12.87
CD4 T cells	Mn^{2+}/Ca^{2+}	0.04+/-0.05	1.69+/-0.87	1.44+/-0.21	0.21+/-0.24	1.02+/-0.12
	EDTA	0.68+/-0.06	1.47+/-0.82	0.83+/-0.23	0.79+/-0.04	0.54+/-0.56
CD8 T cells	Mn^{2+}/Ca^{2+}	0.18+/-0.01	3.97+/-1.98	6.24+/-2.05	0.69+/-0.44	5.61+/-3.32
	EDTA	0.15+/-0.03	3.41+/-1.58	2.15+/-0.47	0.13+/-0.05	1.89+/-0.23
NKT cells	Mn^{2+}/Ca^{2+}	3.30+/-0.54	7.67+/-1.89	15.36+/-3.82	6.82+/-3.17	19.36+/-11.49
	EDTA	1.62+/-1.18	4.70+/-1.38	3.85+/-1.03	0.85+/-0.90	2.96+/-1.10
NK cells	Mn^{2+}/Ca^{2+}	0.02+/-0.08	2.29+/-1.03	4.07+/-1.41	1.56+/-1.33	4.21+/-0.54
	EDTA	0.58+/-0.22	1.07+/-0.50	0.15+/-0.08	0.15+/-0.08	0.50+/-0.22
Neutrophils	Mn^{2+}/Ca^{2+}	0.88+/-0.26	18.35+/-5.60	83.99+/-6.73	3.26+/-1.18	90.22+/-7.74
	EDTA	0.27+/-0.27	7.47+/-2.63	28.44+/-9.06	0.19+/-0.34	47.79+/-25.48
Classical Monocytes	Mn^{2+}/Ca^{2+}	1.85+/-0.61	66.20+/-18.5	85.46+/-6.75	13.78+/-9.13	98.61+/-0.03
	EDTA	1.17+/-1.32	52.80+/-18.7	46.43+/-12.1	7.41+/-6.93	79.92+/-6.12
Activated Monocytes	Mn^{2+}/Ca^{2+}	4.43+/-1.93	66.42+/-17.9	62.65+/-13.8	8.85+/-4.96	97.70+/-0.24
	EDTA	0.49+/-0.10	46.71+/-21.5	31.88+/-12.9	1.51+/-1.19	47.40+/-18.02
mDCs	Mn^{2+}/Ca^{2+}	0.76+/-1.21	32.83+/-9.65	32.76+/-9.70	7.51+/-2.89	27.87+/-9.71
	EDTA	0.18+/-0.22	12.97+/-5.87	12.97+/-5.86	1.03+/-0.49	11.84+/-9.79
pDCs	Mn^{2+}/Ca^{2+}	2.67+/-2.89	26.85+/-13.0	22.57+/-7.30	11.85+/-9.51	14.55+/-4.67
	EDTA	1.55+/-1.37	5.22+/-0.62	2.89+/-0.93	0.0+/-0.0	0.52+/-0.52

Figure 6. Binding of recombinant SARS-CoV Spike proteins to human peripheral blood leukocytes **(A)** Representative flow cytometry histograms of various cell populations prepared from whole blood incubated with labeled recombinant SARS-CoV-2 Spike protein (Trimer), or Spike protein from Kifunensine treated cell (Kif. Tx. Trimer), binding done in the presence of Ca^{2+}/Mn^{2+} or EDTA. **(B)** Percentage of various cell populations prepared from whole blood that bound labelled HKU1 S1 protein (HKU-1 S1), SARS-CoV-2 S1 protein (HCoV-2 S1), SARS-CoV-2 Spike protein (HCoV-2 Trimer), Spike protein purified from Kifunesine treated cells (Kif. Tx. Trimer) or D614G Spike protein. Binding done in the presence of Ca^{2+}/Mn^{2+} or EDTA and assessed by flow cytometry. Background fluorescent (unstained) subtracted from fluorescent signal. Data are from two-eight independent experiments. The recombinant protein that bound the highest % of cells of the different cell types is designated with black outline.

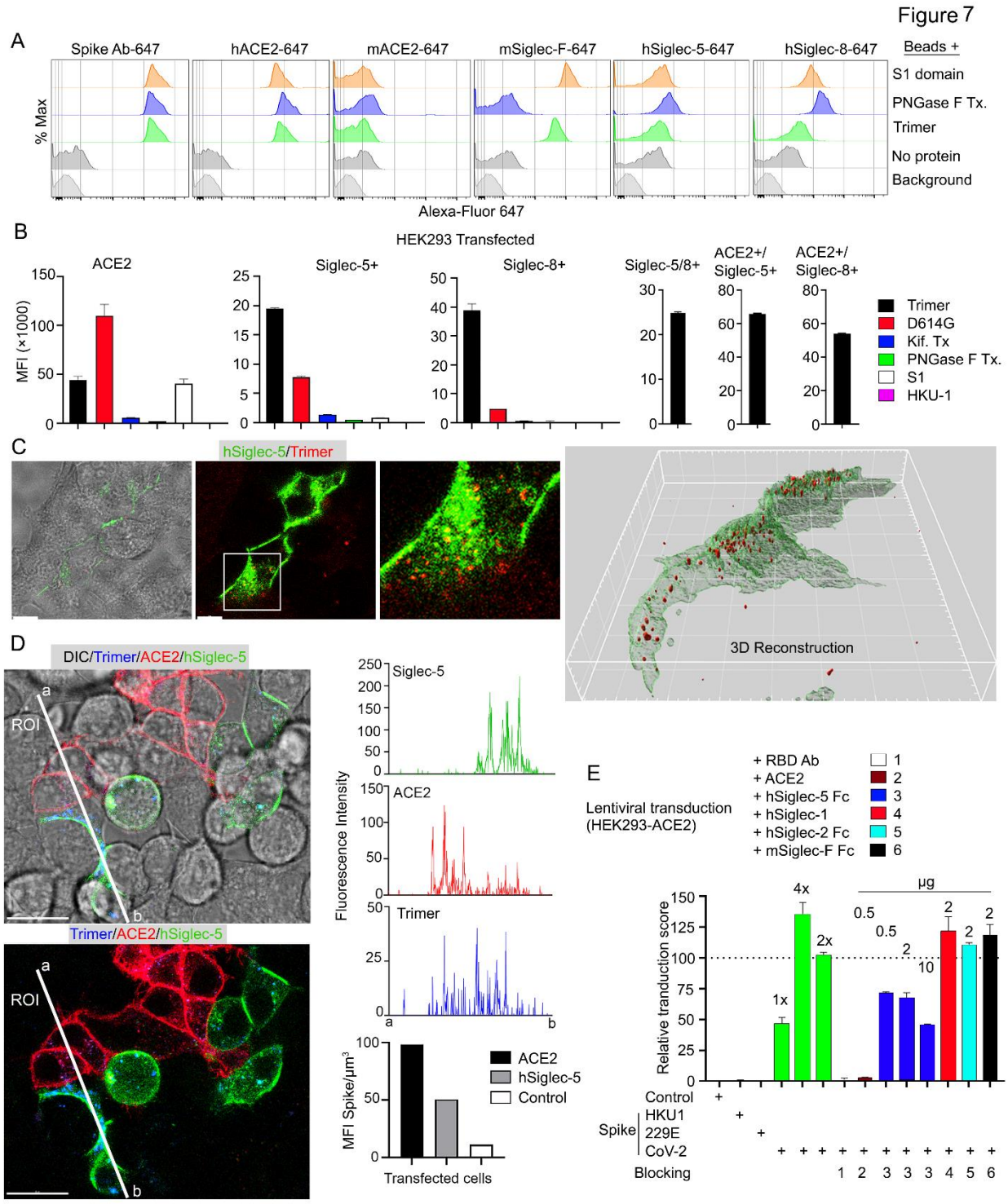

Figure 7. Role of Siglecs in SARS-CoV-2 Spike capture. **(A)** Histograms show mean fluorescence of conjugated recombinant proteins and antibody on nanobeads that are coated with indicated SARS-CoV-2 Spike proteins. Background signal (weak gray) measured with uncoated beads. No protein (gray) means that uncoated beads were incubated with indicated labelled recombinant protein or antibody. **(B)** Flow cytometry assessment of indicated Spike proteins binding to HEK293 cell permanently transfected with

906 ACE2, various Siglecs, or a combination. Dual transfected HEK293 cells noted as Siglec-5/8+,
907 ACE2/Siglec-5+, and ACE2/Siglec-8+. Labelled recombinant proteins were incubated with 5×10^3
908 HEK293 cells on ice for 30 min. Data shown as mean fluorescent intensity. **(C)** DIC and confocal
909 micrographs showing SARS-CoV-2 Spike (Trimer, red) protein acquisition by human Siglec-5-GFP
910 transfected HEK293. ROI-1 in the middle panel is enlarged at the right panel. A 3D-reconstituted volume
911 image of Siglec-5 transfected cell (far right), shows Siglec-5 mediated Spike protein acquisition. Scale bars,
912 30 and 10 μm. **(D)** DIC and confocal images show SARSCoV-2 Spike protein acquisition by human Siglec-
913 5-GFP or ACE2-OFP transfected HEK293. Equal numbers of stable-transfectants expressing Siglec-5-GFP
914 or ACE2-OFP, and non-transfectant were seeded together. Spike protein (Trimer, blue) was added 1 hr prior
915 to imaging. In a region of interest (ROI) line ab fluorescence intensity of Siglec-5-GFP, ACE2-OFP and
916 SARS-CoV-2 Spike trimer were analyzed. Fluorescent intensity graphs show fluorescence intensity of each
917 signal in ROI. Amount of 3Dreconstructed volume of SARS-CoV-2 Spike protein in each stable cell and
918 HEK293 cell were analyzed and plotted in graph. Graphs shows quantity of mean fluorescence intensity of
919 SARS-CoV-2 Spike protein in unit volume (μm^3) of indicated cell types. Scale bars, 20 μm. **(E)**
920 Transduction of Spike protein expressing lentiviruses into ACE2/HEK293 transfectants. Lentiviruses
921 envelop proteins: control (none), human coronavirus HKU1 Spike protein (HKU1), human coronavirus
922 229E Spike protein (229E), and SARS-CoV-2 Spike protein (CoV-2) are indicated. The volume of virus
923 concentrates used for transduction is denoted as 1×, 2×, and 4× on the graph (bright green bars).
924 Transduction scores were normalized to 2× transduction efficiency. Various recombinant proteins or
925 antibody used for inhibition assay are indicated. Recombinant proteins or RBD neutralizing antibody were
926 added 0.5 hr before lentivirus transduction. 3 days later GFP expression was quantitated by flow cytometry.
927 Results are from 3 separate experiments. Statistics, 2x vs 2x + hSiglec-5 Fc (10 μg), $p < 0.0005$.

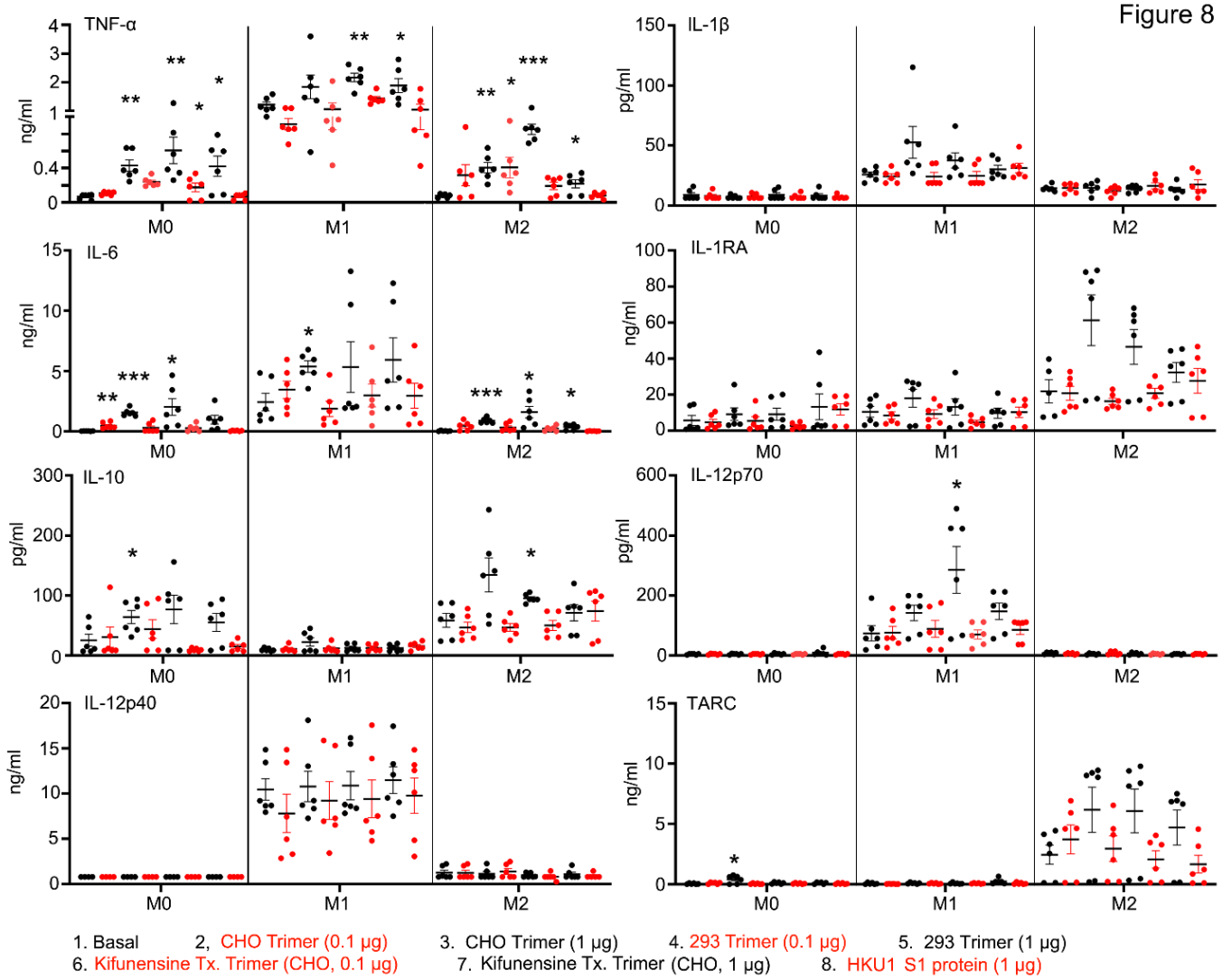

Figure 8. Macrophage cytokine profiles following exposure to different Spike proteins. Quantification of macrophage-associated cytokines in response to indicated Spike proteins. The graph shows the TNF-α, IL1β, IL-6, IL-12p70, IL-12p40, and TARC quantification of M0, M1, or M2 Macrophage cultures following stimulation, or not, with SARS-CoV-2 Spike proteins derived from CHO cells (CHO Trimer; 0.1µg/ml or 1 µg/ml), or 293F cells (293 Trimer; 0.1 µg/ml or 1 µg/ml), or purified Spike protein from Kifunensine treated CHO cells (Kifunensine Tx. Trimer; 0.1 µg/ml or 1 µg/ml), or Human coronavirus HKU1 S1 protein (HKU1 S1 protein; 1 µg/ml) for 48 hr. The error bars denote the mean ± SEM. Two-way ANOVA was used to compare treated samples to basal M0, M1, or M2 population ($n = 6$, $*p < 0.05$; $**p < 0.01$; $***p < 0.001$).

937 **Supplementary Material**

938

939 **Figure 1-figure supplement 1.** Preparation of SARS-CoV-2 proteins.

940

941 **Figure 1-figure supplement 2.** Confocal micrographs were taken for staining control and to analyze
942 neutrophil fragmentation caused by SARS-CoV-1 Spike VLPs, comparing them to delta Env VLPs.

943

944 **Figure 2-figure supplement 1.** Intranasal SARS-CoV-2 Spike protein administration to K18-hACE2
945 mice.

946

947 **Figure 3-figure supplement 1.** Quantification of lung permeability and neutrophil recruitment.

948

949 **Figure 4-figure supplement 1.** Quantification of neutrophil count in cremaster muscle.

950

951 **Figure 4-figure supplement 2**. Localization of Spike protein in the liver following intravenous
952 administration.

953

954 **Figure 4-figure supplement 3.** Localization of SARS-CoV-2 Spike protein at other sites following
955 intravenous injection and subcutaneous injection near the inguinal lymph node.

956

957 **Video 1.** Local Spike protein injection results in neutrophil recruitment in the cremaster muscle.

958

959 **Video 2.** Local injection of Spike proteins causes neutrophil fragmentation.

960

961 **Video 3.** Intravenously injected Spike protein outlines liver sinusoids and accumulates on Kupffer cells.

962

963 **Video 4.** Neutrophils undergo NETosis when plated on A549 cells in the presence of Spike protein.

964

965 **Video 5.** hSiglec-5 expressing HEK293 cells bind and endocytosis Spike protein.

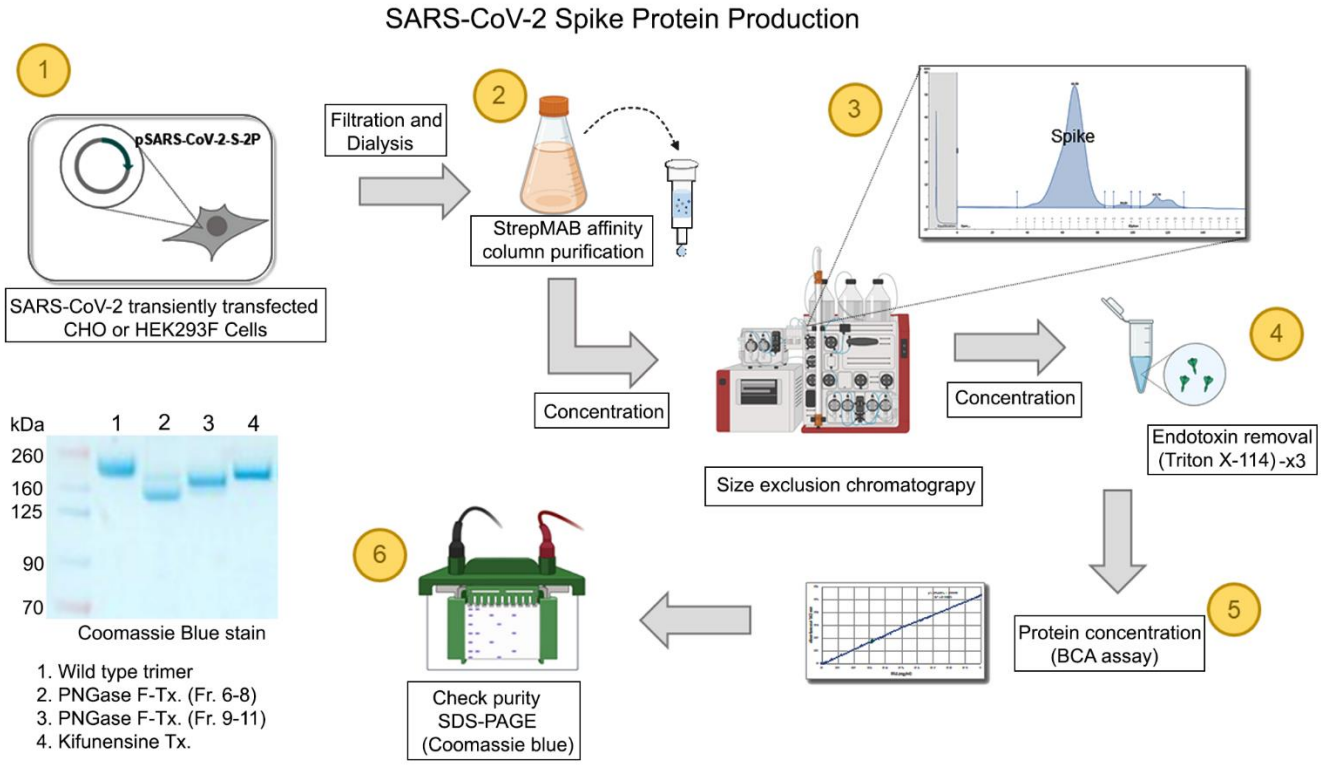

Figure 1-figure supplement 1. Preparation of SARS-CoV-2 proteins. Outline of recombinant proteins production and purification from cultured media of pSARS-CoV-2-S-2P transfected CHO or HEK293F cells. See methods for PNGase F and Kifunensine treatment. Calculated molecular weights: wild type trimer -210 kDa, PNGase F-Tx. (Fr. 6-8)- 146 kDa, PNGase F-Tx (Fx. 9-11)-178 kDa, and Kifunensine Tx.- 197.5 kDa.

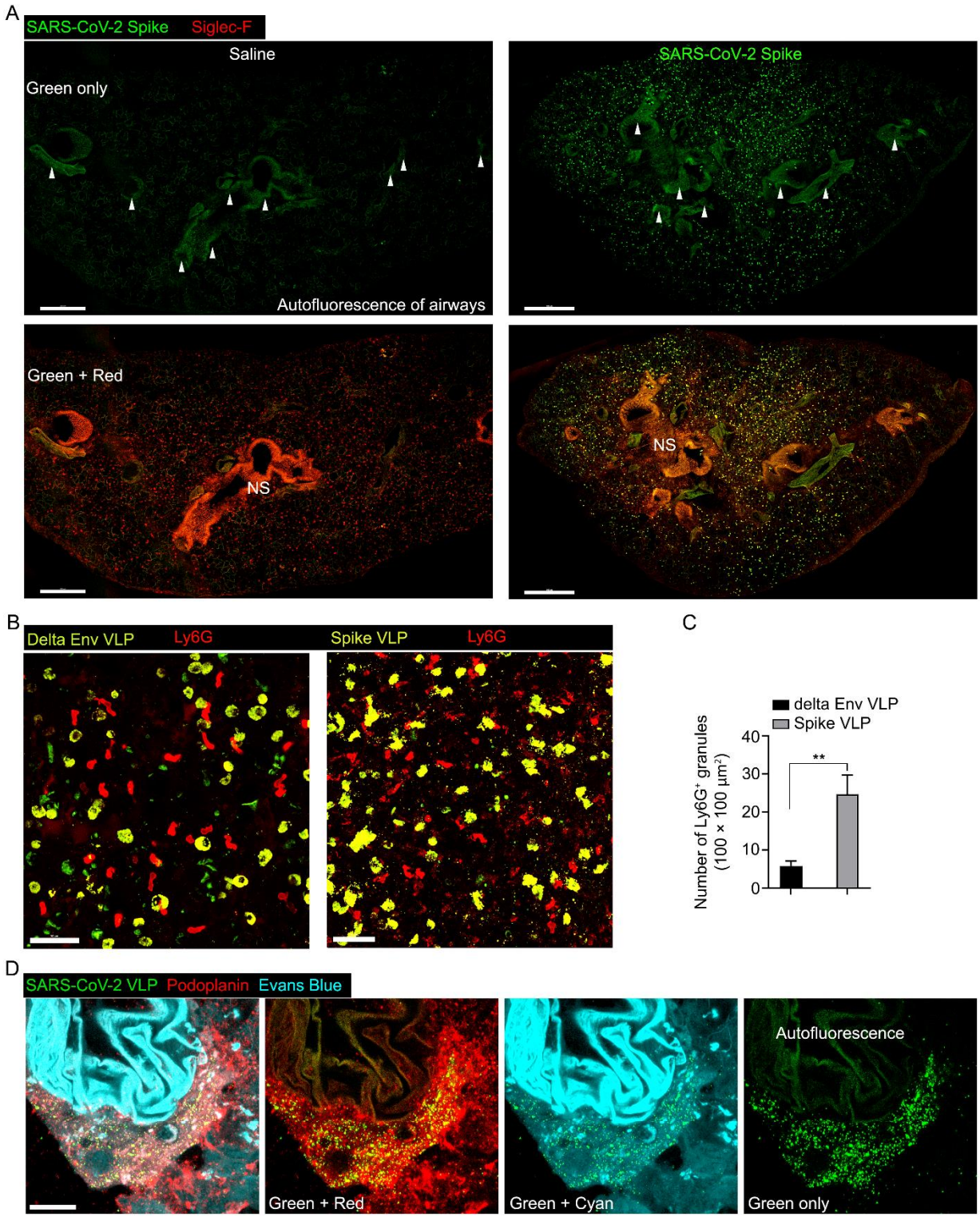

Figure 1-figure supplement 2. Confocal micrographs were taken for staining control and to analyze neutrophil fragmentation caused by SARS-CoV-1 Spike VLPs, comparing them to delta Env VLPs. **(A)** Confocal micrographs compare the negative control (saline) with the positive sample (SARS-CoV-2 Spike, Alexa Fluor 488). Arrowheads in the upper panels indicate autofluorescence background. The nonspecific

976 Siglec-F antibody stain background is denoted as 'NS' in the lower panels. Scale bars, 500 μm. **(B)** Confocal
977 micrographs of lungs collected at 3 hours post instillation of SARS-CoV-2 Spike protein (left) or delta
978 envelope (right) VLP (green, GFP) are shown. Infiltrated neutrophils (red, Ly6G) in lung tissue were
979 visualized. Scale bars, 50 μm. (**C**) Neutrophil fragmentation was measured by counting the Ly6G+ granules
980 in five different areas of 100 × 100 μm² each. ** $p < 0.01$, paired t-test. (**D)** A confocal micrograph shows
981 a lung lymphatic vasculature visualized with Podoplanin antibody. Fifty microliters of a mixture of Evans
982 blue (cyan) (5 μg) and Spike bearing VLPs (green) (0.5 million counts) were applied to the mouse nose.
983 The first panel presents the merged image of all signals, while the subsequent panels display specific color
984 combinations: green and red in the second, and green and cyan in the third. The fourth panel exclusively
985 exhibits the green signal, with autofluorescence of the lung airway structure indicated. Scale bars, 20 μm.

A K18-hACE2 Tg 3 hr post Trimer instillation

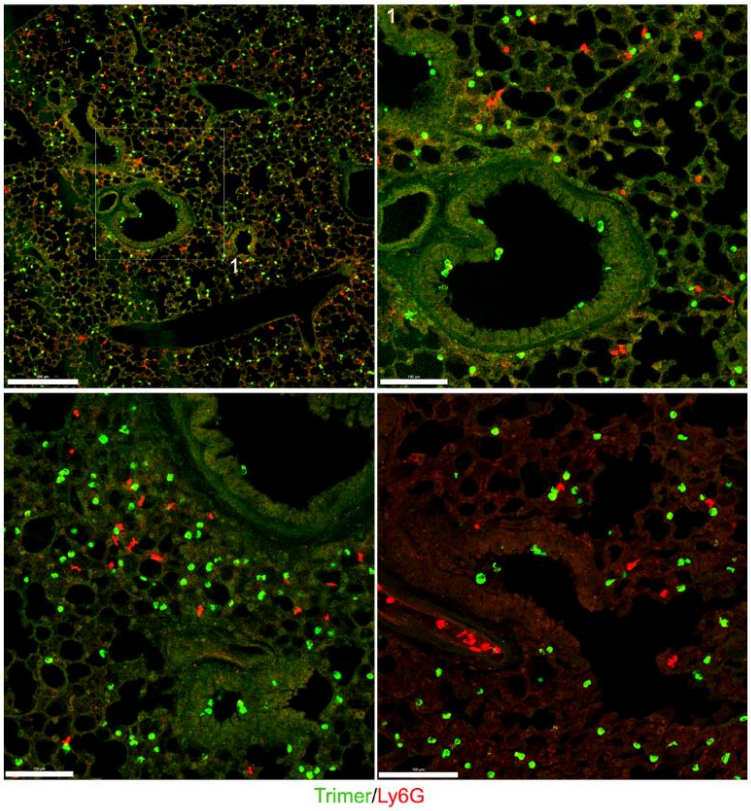

B

	JAX 664	JAX 034860 K18-hACE2
	Spike Trimer (CHO) (n=6)	Spike Trimer (CHO) (n=3)
Neutrophils	3.395 ± 0.916	3.507 ± 0.360
rMono	2.888 ± 0.759	6.830 ± 1.264***
iMono	3.565 ± 0.805	5.257 ± 0.828
AMac	77.467 ± 5.924	87.867 ± 2.609 **
iMac1	9.288 ± 3.234	6.577 ± 0.897
iMac2	13.583 ± 3.234	10.157 ± 0.645
iMac3	31.800 ± 7.223	11.477 ± 1.119 ***
Eosinophils	2.008 ± 0.539	3.803 ± 0.354
CD11b+DC	5.962 ± 1.136	10.497 ± 1.206 ***
CD11b-DC	3.702 ± 0.633	6.667 ± 0.750 **
NK&NKT	1.110 ± 0.176	3.623 ± 0.333 *
B	1.055 ± 0.196	2.403 ± 0.193
T	1.015 ± 0.360	2.710 ± 0.308

Figure 2-figure supplement 1. Intranasal SARS-CoV-2 administration to K18-hACE2 mice. (**A**) Representative confocal images of lung sections 3h post intranasal SARS-CoV-2 Spike protein (3 µg, green). Neutrophils immunostained with Ly6G. (**B**) SARS-CoV-2 Spike protein uptake by lung leukocytes 18 hr following intranasal inoculation. Flow cytometry results from analysis of leukocytes purified from the lungs of WT or K18-hACE2 mice. Data for JAX 664 mice same as shown in figure 2. K18-hACE2 leukocyte values significantly different from those from the JAX 664 mice are indicated, *$p < 0.05$; **$p < 0.01$; ***$p < 0.001$.

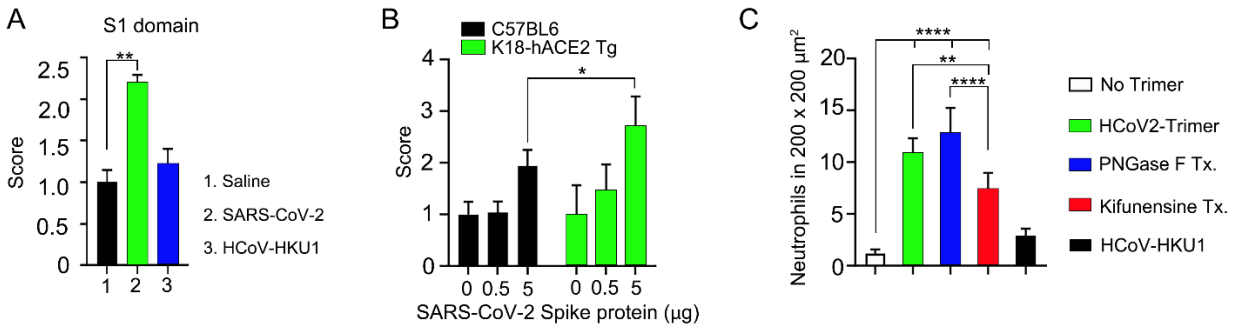

Figure 3-figure supplement 1. Quantification of lung permeability and neutrophil recruitment. **(A)** Evans blue (200 µl of 5 mg/ml in PBS) was intravenously injected 1.5 hours after intranasal Spike administration. The indicated recombinant proteins' S1 domains (3 µg per mouse) were administered. Lungs were collected 1 hour after Evans blue injection. The score was calculated based on the amount of Evans blue dye (in µg/g) in the lungs administered with the Spike protein, divided by the average amount of Evans blue dye in lungs administered with saline. ** $p < 0.01$, One-way ANOVA. **(B)** The permeability of lung vasculature was measured by comparing wild-type mice with K18-hACE2 transgenic mice. The SARS-CoV-2 Spike protein was administered at two different concentrations: 0.5 µg or 5 µg per mouse. * $p < 0.05$, Two-way ANOVA. **(C)** The number of neutrophils was counted in six different areas, each measuring 200 × 200 µm². ****$p < 0.0001$, One-way ANOVA.

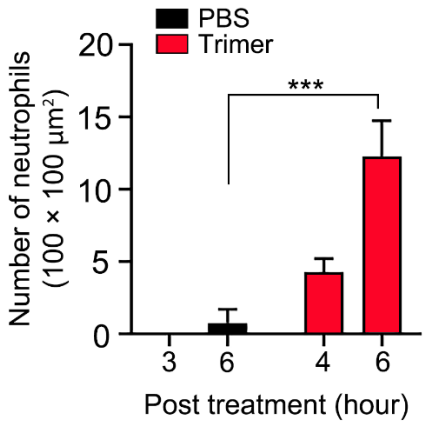

1004

1005 **Figure 4-figure supplement 1**. Quantification of neutrophil count in cremaster muscle. The number of

1006 neutrophils was counted in four 100 × 100 μm² areas. ***$p < 0.001$, Two-way ANOVA.

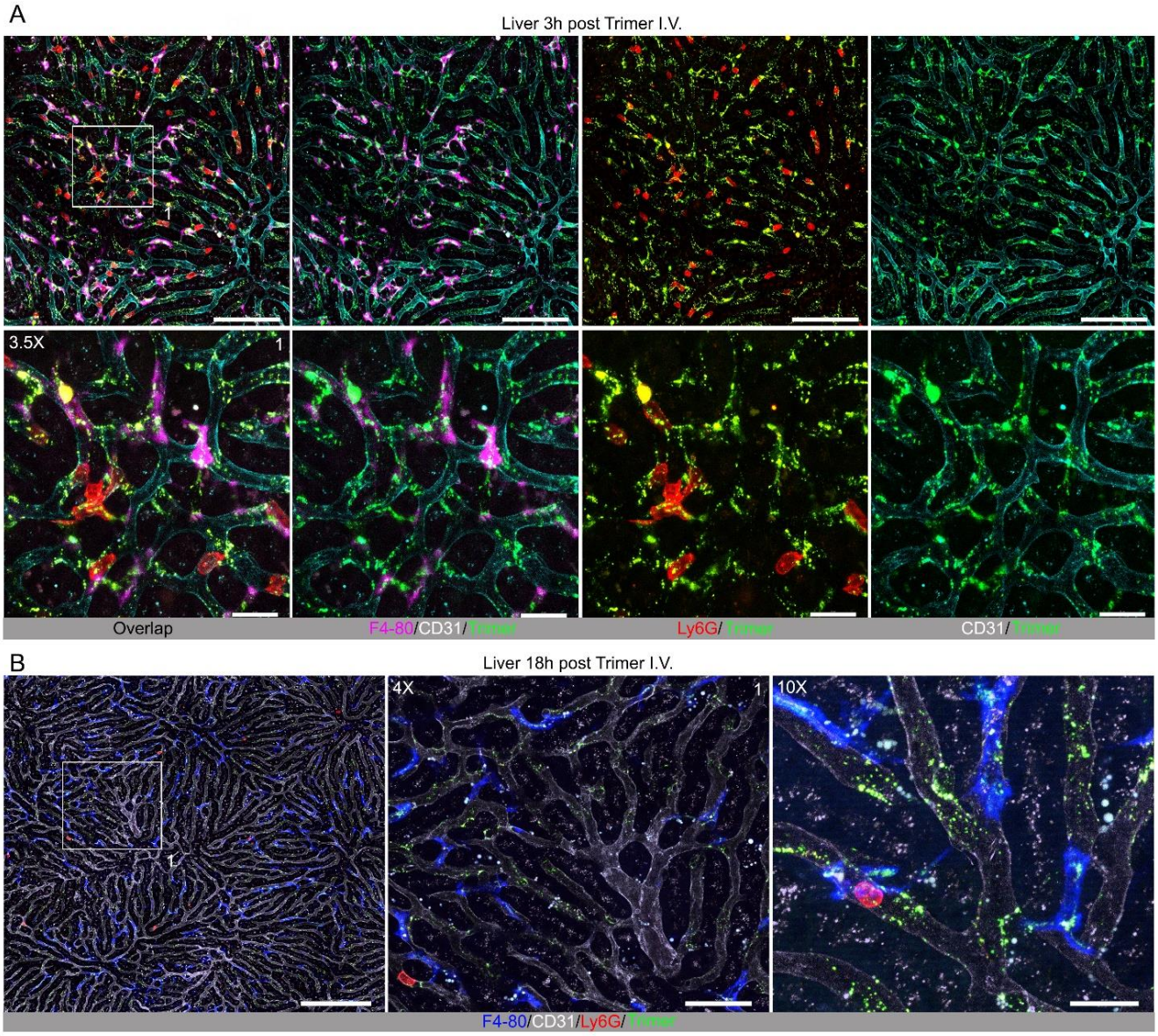

Figure 4-figure supplement 2. Localization of Spike protein in the liver following intravenous administration. **(A)** Confocal micrographs of the liver imaged at 3 hr post intravenous injection of SARS-CoV-2 Spike (Trimer) protein. Spike protein (green), Kupffer cells (magenta, F4/80), and neutrophils (red, Ly6G) shown in liver sinusoid vasculature (cyan, CD31). Antibodies injected 0.3 hr before imaging. ROI-1 (box) (upper left) is enlarged (3.5× magnification) in lower panels. Scale bars, 100 and 20 μm. **(B)** Confocal micrographs of liver imaged at 18 hr post intravenous injection of SARS-CoV-2 Spike protein. Spike protein (green), Kupffer cells (blue, F4/80), and neutrophils (red, Ly6G) are shown in liver sinusoid vasculature (white, CD31). Antibodies injected 0.3 hr before imaging. ROI-1 (box) (left) is enlarged in the middle panel (4× magnification). Enlarged image shows neutrophil contacting Spike protein bearing cells on liver sinusoid endothelium (10× magnification). Scale bars, 200, 50, and 20 μm.

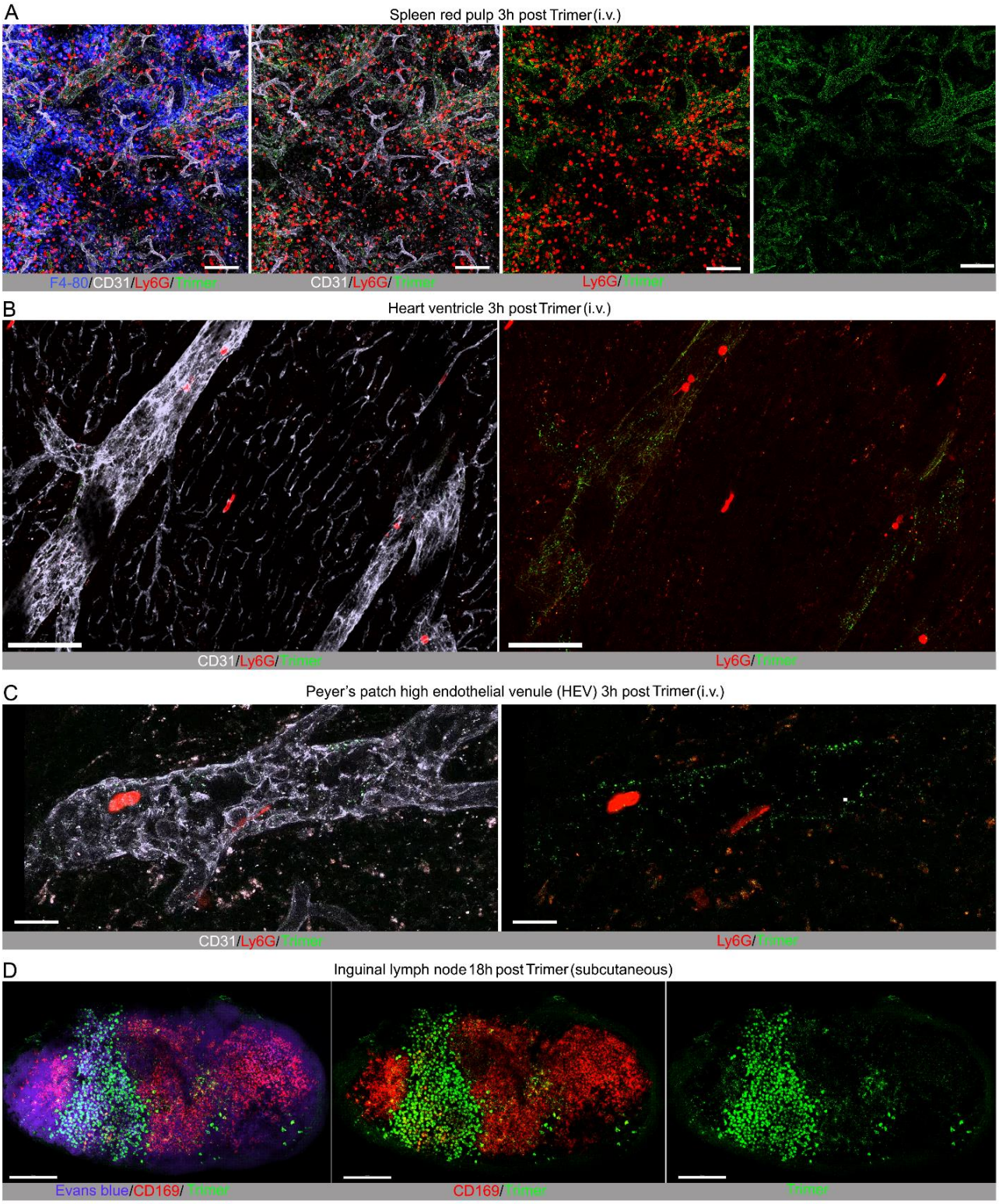

1017 **Figure 4-figure supplement 3**. Localization of SARS-CoV-2 Spike protein at other sites following
1018 intravenous injection and subcutaneous injection near the inguinal lymph node. **(A)** Confocal micrographs
1019 of mouse spleen imaged 3 hr post intravenous injection of SARS-CoV-2 Spike (Trimer) protein. Spike

1020 protein (green), red pulp macrophages (blue, F4/80), and neutrophils (red, Ly6G) visualized in spleen red
1021 pulp vasculature (cyan, CD31). Antibodies injected 1 hr before imaging. Scale bars, 100 µm. (**B)** Confocal
1022 micrographs of heart ventricle imaged 3 hr post intravenous injection of Spike protein. Spike protein (green)
1023 and neutrophils (red, Ly6G) localized in heart blood vessels (white, CD31). Antibodies injected 1 hr before
1024 imaging. Scale bars, 100 µm. (**C)** Confocal micrographs of Peyer's patch high endothelial venules (HEV)
1025 imaged at 3 hr post iv injection of Spike protein. Spike protein (green) and neutrophils (red, Ly6G) shown
1026 in HEV (white, CD31). Antibodies injected 0.5 hr before imaging. Scale bars, 20 µm. (**D)** Confocal
1027 micrographs of inguinal lymph node imaged at 18 hr post tail base injection of Spike protein. Spike protein
1028 (green) and subscapular sinus macrophages (red, CD169) shown. Subcapsular sinus defined via Evans blue
1029 (purple) signal. Antibodies and Evans blue injected 1 hr before imaging. Scale bars, 200 µm.

1030 **Video Legends.**

1031

1032 **Video 1.** Local Spike protein injection results in neutrophil recruitment in the cremaster muscle. Confocal
1033 intravital microscopy movie shows neutrophils (green), platelets (red), endothelium (blue) immunostained
1034 with Alexa Fluor 488-Gr1, DyLight 649-GP1bβ, and Alexa Fluor 555-CD31 monoclonal antibodies,
1035 respectively. Intrascrotal injection of PBS or Spike protein (5 μg) 3-4 hours prior to imaging. The first
1036 sequence spans a ~60 min (PBS) while the second sequence spans a ~45 min (Spike) imaging period.
1037 Images were captured at ~1 frame per 30s with ~100× magnification. Time counter is hour:minute:second.

1038

1039 **Video 2.** Local injection of Spike proteins causes neutrophil fragmentation. Confocal intravital microscopy
1040 movie shows neutrophils (green), platelets (red), endothelium (blue) immunostained with Alexa Fluor
1041 488Gr1, Dylight 649-GP1bβ, and Alexa Fluor 555-CD31 monoclonal antibodies, respectively. Intrascrotal
1042 injection of Il-1β or Il-1β plus 5 μg Spike protein ~20 hours prior to imaging. Both sequences span a 20
1043 min period. Images were captured at ~1 frame per 30s with ~100× magnification. Time counter is
1044 hour:minute:second.

1045

1046 **Video 3.** Intravenously injected Spike protein outlines liver sinusoids and accumulates on Kupffer cells.
1047 The liver imaging was taken at three different time points; from 20 min to 1hr, from 1hr 10 min to 1hr 15
1048 min, and from 1hr 25 min to 46 min after SARS-CoV-2 Spike protein (green, Alexa Fluor 488) injection.
1049 An image sequence of a 12 μm z-projection was acquired with 40× lens as scanning speed of 11.05 sec
1050 between frames. Kupffer cells (magenta, F4/80), and neutrophils (red, Ly6G) in liver sinusoid vasculature
1051 (cyan, CD31) were visualized with antibody injection into tail vein at 30 min prior to imaging. The scale
1052 bar represents 20 μm. Time counter is hour:minute:second.

1053

1054 **Video 4.** Neutrophils undergo NETosis when plated on A549 cells in the presence of Spike protein. A549
1055 cells were plated on chamber slide 48 hr before trimer treatment. SARS-CoV-2 Spike trimer (green) was
1056 added to A549 cell culture 24 hr before neutrophil seeding. Purified human neutrophils stained with Hoechst
1057 (cyan) and were seeded on A549 cells in propidium iodide (PI, 1 μg/ml) containing culture media. NETosis
1058 of neutrophils were detected by exposed DNA (red, PI). An image sequence of a 20 μm zprojection was
1059 acquired with 40× lens at a scanning speed 1 frame /10 min over 5 hours. Regions of interest (Box A and
1060 B) demonstrate a typical NETosis of neutrophil contacting on trimer bearing A549 cell were enlarged in
1061 second part of video. Scale bars, 30 and 10 μm. Time banner, hour:minute:second.

1062

1063 **Video 5.** hSiglec-5 expressing HEK293 cells bind and endocytosis Spike protein. Individually established
1064 stable-transfected cells expressing Siglec-5-GFP or ACE2-OFP were plated in the same chamber slide with
1065 non-transfection cells. After overnight culture SARS-CoV-2 Spike protein (1 μg/ml) was overlaid for 1 hr
1066 before imaging. An image sequence of a 3 μm z-projection was acquired with 40× lens at a scanning speed
1067 of 23 sec between frames. Signals visualized as SARS-CoV-2 Spike trimer (blue), Siglec-5-GFP (green),
1068 ACE2-OFP (red), and non-transfected HEK293 cells (gray). The scale bar represents 20 μm. Time counter
1069 is hour:minute:second.

1070 Reagent Table

Designation	**Catalog Number**	**SOURCE**	**IDENTIFIER**
Cell line			
FreeStyle™ CHO-S Cells	R80007	ThermoFisher Scientific	
FreeStyle™ 293-F Cells	R79007	ThermoFisher Scientific	
293T	CRL-3216™	ATCC	
293 [HEK-293]	CRL-1573™	ATCC	
A549	CRM-CCL-185™	ATCC	
Mice			
C57BL/6J	Jax stock 000664	Jackson Lab.	IMSR_JAX:000664
K18-hACE2 (B6.Cg- Tg(K18- ACE2) 2Prlmn/J)	Jax stock 034860	Jackson Lab.	IMSR_JAX:034860
Antibodies			
PerCP-Cy™5.5 Rat Anti-Mouse Ly6G	560602	BD Biosciences	RRID : AB_1727563
PE-Cy™7 Rat Anti-Mouse Ly6G	560601	BD Biosciences	RRID: AB_1727562
PE Rat Anti-Mouse I-A/I-E	557000	BD Biosciences	RRID: AB_396546
PE/Cyanine7 anti-mouse CD24 Antibody	101822	BioLegend	RRID: AB_756048
PerCP/Cyanine5.5 anti-mouse CD24 Antibody	101824	BioLegend	RRID: AB_1595491
Alexa Fluor® 647 anti-mouse CD64 (FcγRI) Antibody	139322	BioLegend	RRID: AB_2566561
Alexa Fluor® 488 anti-mouse CD31 Antibody	102414	BioLegend	RRID: AB_493408

Alexa Fluor® 594 anti-mouse CD31 Antibody	102432	BioLegend	RRID: AB_2617017
APC-Cy™7 Rat Anti-Mouse Siglec-F	565527	BD Biosciences	RRID: AB_2732831
PE anti-mouse CD170 (Siglec-F) Antibody	552126	BD Biosciences	RRID: AB_394341
Alexa Fluor® 647 Rat Anti-Mouse Siglec-F	562680	BD Biosciences	RRID: AB_2687570
BV421 Rat Anti-Mouse Ly6C	562727	BD Biosciences	RRID: AB_2737748
Brilliant Violet 650™ anti-mouse/human CD11b Antibody	101259	BioLegend	RRID: AB_2566568
Brilliant Violet 711™ anti-mouse CD45 Antibody	103147	BioLegend	RRID: AB_2564383
Brilliant Violet 785™ anti-mouse CD11c	117336	BioLegend	RRID: AB_2565268
PE/Dazzle™ 594 anti-mouse CD19 Antibody	115554	BioLegend	RRID: AB_2564001
Brilliant Violet 421™ anti-mouse F4/80 Antibody	123137	BioLegend	RRID: AB_2563102
PE anti-mouse CD169 (Siglec-1) Antibody	142404	BioLegend	RRID:AB_10915697
PE anti-human CD16 Antibody	360704	BioLegend	RRID: AB_2562749
PE/Cyanine7 anti-human CD56 (NCAM) Antibody	362510	BioLegend	RRID: AB_2563927
APC Mouse Anti-Human CD4	551980	BD Bioscience	RRID: AB_398521
APC/Cyanine7 anti-human CD8a Antibody	301015	BioLegend	RRID: AB_314134
Brilliant Violet 421™ anti-human HLA-DR Antibody	307635	BioLegend	RRID: AB_2561831

Brilliant Violet 650™ anti-human CD14 Antibody	301836	BioLegend	RRID: AB_2563799
PerCP-Cy™5.5 Mouse Anti-Human CD14	550787	BD Bioscience	RRID: AB_393884
V500 Mouse Anti-Human CD14	561391	BD Bioscience	RRID: AB_10611856
Brilliant Violet 711™ anti-human CD20 Antibody	302341	BioLegend	RRID: AB_2562602
PE/Cyanine7 anti-human CD20 Antibody	302312	BioLegend	RRID: AB_314260
Alexa Fluor® 700 anti-human CD20 Antibody	302322	BioLegend	RRID: AB_493753
PE anti-human CD123 Antibody	306006	BioLegend	RRID: AB_314580
APC/Cyanine7 anti-human CD15 (SSEA-1) Antibody	323048	BioLegend	RRID: AB_2750190
APC anti-human CD66b Antibody	305118	BioLegend	RRID: AB_2566607
Brilliant Violet 421™ anti-human CD11c Antibody	337226	BioLegend	RRID: AB_2564485
BD Pharmingen™ PerCP-Cy™5.5 Mouse Anti-Human CD3	552852	BD Biosciences	RRID: AB_394493
PE Mouse Anti-Human CD22	562859	BD Bioscience	RRID: AB_2737845
APC anti-human CD170 (Siglec-5) Antibody	352005	BioLegend	RRID: AB_2564262
APC anti-human Siglec-8 Antibody	347106	BioLegend	RRID: AB_2561402

Alexa Fluor® 647 anti-mouse CD169 (Siglec-1) Antibody	142408	BioLegend	RRID: AB_2563621
Human Siglec-8 Antibody	MAB7975	R & D Systems	
Human Siglec-8 PE-conjugated Antibody	FAB7975P	R & D Systems	RRID: AB_2905537
Human Siglec-1/CD169 Alexa Fluor® 647-conjugated Antibody	FAB5197R100UG	R & D Systems	RRID: AB_2905550
Human ACE-2 Alexa Fluor® 647-conjugated Antibody	FAB9332R100UG	R & D Systems	
Human Siglec-8 Alexa Fluor® 750conjugated antibody	FAB7975S-100UG	R & D Systems	
Human ACE-2 Alexa Fluor® 405-conjugated Antibody	FAB9332V-100UG	R & D Systems	
Human/Mouse/Rat/Hamster ACE-2 Antibody	AF933	R & D Systems	RRID: AB_355722
Mouse ACE-2 Antibody	AF3437	R & D Systems	RRID: AB_2223140
SARS-CoV-2 (2019-nCoV) Spike Neutralizing Antibody, Rabbit Mab	40592-R001	SinoBiological	RRID: AB_2857936
Rat IgG derivative against the GPIbβ subunit of the murine platelet/megakaryocyte-specific GPIb-V-IX complex antibody	X647	Emfret	RRID: AB_2861336
Mouse LYVE-1 Antibody	MAB2125	R & D Systems	RRID: AB_2138528
PE anti-mouse Podoplanin Antibody	127408	BioLegend	RRID: AB_2161928
Buffer and chemicals			
LIVE/DEAD™ Fixable Aqua Dead Cell Stain Kit	L34966	Thermo Fisher Scientific	

Evans Blue	E2129-10G	Sigma-Aldrich	
Propidium Iodide (PI)	P4864- 10ML	Sigma-Aldrich	
FluoSpheres™ NeutrAvidin™-Labeled Microspheres, 0.2 µm, yellow-green fluorescent (505/515), 1% solids	F8774	Thermo Fisher Scientific Inc.	
2M MgCl2	340-034-721	Quality Biological Inc.	
2M CaCl2	351-130-721	Quality Biological Inc.	
HBSS wo Ca2+&Mg2+	14175-095	Thermo Fisher Scientific Inc.	
Albumin, Bovine Serum, Fraction V, Fatty Acid-Poor, Endotoxin-Free	126579-100GM	Sigma-Aldrich	
5M NaCl	351-036-101	Quality Biological Inc.	
2M Tris-HCl, pH8.0	351-092-101	Quality Biological Inc.	
1X PBS wo Ca2+ & Mg2+	114-058-101	Quality Biological Inc.	
0.5M EDTA, pH8.0	351-027-101	Quality Biological Inc.	
Manganese (II) chloride tetrahydrate	63535-50G-F	Sigma-Aldrich	
Liberase™ TL(Thermolysin Low) Research Grade	5401020001	Roche Applied Science	
DNase I	10104159001	Roche Applied Science	
Cover glass	Cover glass – #4860-1D	Brain Research Laboratories	

Universal Mounting Frame AK-Set		PECON	
Opti-MEM™	31985070	Thermo Fisher Scientific Inc.	
RPMI 1640 Media	11875093	Thermo Fisher Scientific Inc.	
TransIT-293 Transfection Reagent	MIR 2704	Mirus Bio LLC	
Lenti-X™ Concentrator	631232	Takara Bio USA Inc.	
FreeStyle™ 293 Expression Medium	12338018	Thermo Fisher Scientific Inc.	
FreeStyle™ CHO Expression Medium	12651014	Thermo Fisher Scientific Inc.	
Plasmids			
SIGLEC5 (NM_003830) Human Tagged ORF Clone	RC206610	Origene	
SIGLEC5 (NM_003830) Human Tagged ORF Clone	RG206610	Origene	
Human Siglec-8 (NP_055257) VersaClone cDNA	RDC1496	Origene	
SARS-CoV-2 Spike-S			
HIV-1 NL4-3 Gag-iGFP ΔEnv	12455	NIH AIDS Reagent Program	
Human Coronavirus Spike glycoprotein Gene ORF cDNA clone expression plasmid(Codon Optimized) HCoV-HKU1	VG40021- UT	SinoBiological	
Human coronavirus(HCoV-229E) Spike Gene ORF cDNA clone expression plasmid(Codon Optimized) HCoV-229E	VG40605- UT	SinoBiological	
ACE2 cDNA ORF Clone, Human, C-OFPSpark® tag	HG10108-ACR	SinoBiological	

pCMV-dR8.2 dvpr	8455	Addgene	
pLentipuro3 TO V5-GW EGFP-Firefly Luciferase	119816	Addgene	
Recombinant Protein			
ACE2 Protein, Human, Recombinant (mFc Tag)	10108-H05H	SinoBiological	
Human coronavirus HKU1 (isolate N5) (HCoV-HKU1) Spike/S1 Protein (S1 Subunit, His Tag)	40602-V08H	SinoBiological	
Human coronavirus (HCoV-229E) Spike Protein (S1+S2 ECD, His Tag)	40605-V08B	SinoBiological	
SIGLEC5 Protein, Human, Recombinant (hFc Tag)	11798-H02H	SinoBiological	
Recombinant Mouse Siglec-F Fc Chimera Protein, CF	1706-SF-050	R & D Systems	
Recombinant Human Siglec-8 Fc Chimera Protein, CF	9045-SL-050	R & D Systems	

1071